Chapter 12
Energy Harvesting from the Fuel Cell Hybrid Power Source Based on Extremum Seeking Control Schemes

Nicu Bizon

Abstract Energy harvesting is known as the conversion process of ambient energy into usable electrical energy, including the available and free energy of the renewable and green energy sources. This chapter analyzes the possibility to use the Extremum Seeking Control schemes for harvesting the hydrogen energy via a Fuel Cell Hybrid Power Source. The new Extremum Seeking Control schemes proposed here are based on a band-pass filter with the frequencies' band larger than that of the series combination of high-pass and low-pass filters used in the classical Extremum Seeking Control scheme. The mathematical modeling of the Extremum Seeking Control scheme that is applied to nonlinear dynamic plant shows the close relations between the search speed, the derivatives of the unknown input-to-output map, and the cut-off frequencies of the band-pass filter. The simulation results are compared with the results of classical Extremum Seeking Control schemes. The ratio of these search speeds is used as the performance indicator, besides the tracking accuracy evaluated for each control scheme. A Maximum Power Point tracking technique is proposed for the Fuel Cell stack based on a modified Extremum Seeking Control that slightly improves the performance. A higher value of the searching speed is obtained for the same tracking accuracy. The search speed will increase proportionally with the product of both control parameters (the closed loop gain and the dither gain), so it is practically limited for safe reasons. An advanced Extremum Seeking Control scheme is proposed here to further reduce the power ripple and obtain the imposed performance related to the search speed and tracking accuracy. Finally, the dynamical operation of the Fuel Cell stack under constant and variable load is shown.

N. Bizon (✉)
Department of Electronics, Computers and Electrical Engineering,
University of Pitesti, Pitesti, Romania
e-mail: nicu.bizon@upit.ro

N. Bizon
University Politehnica of Bucharest, Bucharest, Romania
e-mail: nicubizon@yahoo.com

N. Bizon et al. (eds.), *Energy Harvesting and Energy Efficiency*,
Lecture Notes in Energy 37, DOI 10.1007/978-3-319-49875-1_12

Keywords Fuel cell hybrid power source (FCHPS) · Extremum seeking control (ESC) · Maximum power point (MPP) · Search speed · Tracking accuracy · FC system · Energy harvesting

Abbreviation and Acronyms

aESC	advanced Extremum Seeking Control
ANN	Artificial Neural Network
BPF	Band Pass Filter
bpfESC	Band Pass Filter ESC
EA	Evolutionary Algorithms
ES	Energy Sources
ESS	Energy Storage System
EQ	Equivalent
ESC	Extremum Seeking Control
FC	Fuel Cell
FCHPS	Fuel Cell Hybrid Power Source
FLC	Fuzzy Logic Controller
GMPP	Global Maximum Power Point
GMPPT	GMPP Tracking
HF	High Frequency
hoESC	high-order Extremum Seeking Control
HPF	High-Pass Filter
HC	Hill Climbing
HPS	Hybrid Power Source
H_1	First Harmonic
IC	Incremental Conductance
LF	Low Frequency
LPF	Low-Pass Filter
MEP	Maximum Efficiency Point
MPP	Maximum Power Point
MPPT	MPP Tracking
mESC	modified Extremum Seeking Control
P&O	Perturb & Observe
PEM	Proton Exchange Membrane
PV	Photovoltaic
RCC	Ripple Correlation Control
RES	Renewable Energy Sources
WT	Wind Turbines

12.1 Introduction

In general, the conversion process of ambient energy into usable electrical energy using Renewable Energy Sources (RESs), such as Photovoltaic (PV) panels, and Wind Turbines (WT), or on hydrogen energy via a Fuel Cell (FC) stack can be modeled by a nonlinear dynamic plant having an unknown input-to-output map, $y = f(x)$ with one or more maximums. Usually, one Maximum Power Point (MPP) appears in the stationary regime and more local extremes appear on the power profile during transitory regimes. The control variable used for searching the MPP or global MPP (GMPP) is the current or the voltage, or the power generated by the RESs [1, 2] (see Fig. 12.1). Note, that the GMPP must be accurately tracked in dynamic regime, too [3, 4].

The Fuel Cell Hybrid Power Source (FCHPS) architecture which will be analyzed in this chapter (see Sect. 12.6) is based on the generic Hybrid Power Source (HPS) architecture shown in Fig. 12.1. Note that the FC stack will be connected to the ESS bus by a unidirectional DC-DC converter that is controlled using a Maximum Power Point (MPP) tracking or a Maximum Efficiency Point (MEP) algorithm. The MPP tracking (MPPT) controller will control the FC power flow acquiring the samples of FC current and FC voltage (which are noted with iFC and vFC in Fig. 12.1). The MPP of the FC stack under different fuelling modes will be tracked using the Extremum Seeking Control (ESC) based on adaptive dithering action of the reference current (iref) (see Fig. 12.2). The reference current is compared to the FC current to generate the switching pulses based on an appropriate current-mode control strategy.

The MPP tracking (MPPT) algorithms and GMPP tracking (GMPPT) algorithms were extensively analyzed in last decade, starting with the required applications developed for an array of PV panels [5]. In general, some 1-D models were used to

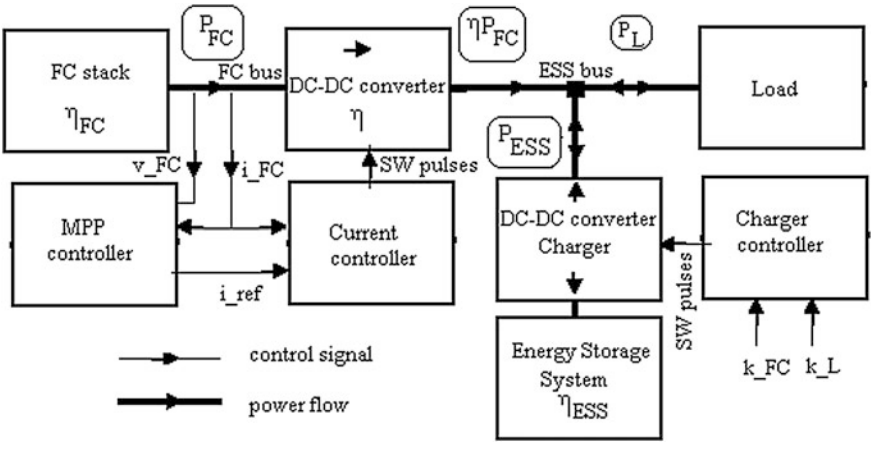

Fig. 12.1 Architecture of the fuel cell hybrid power source

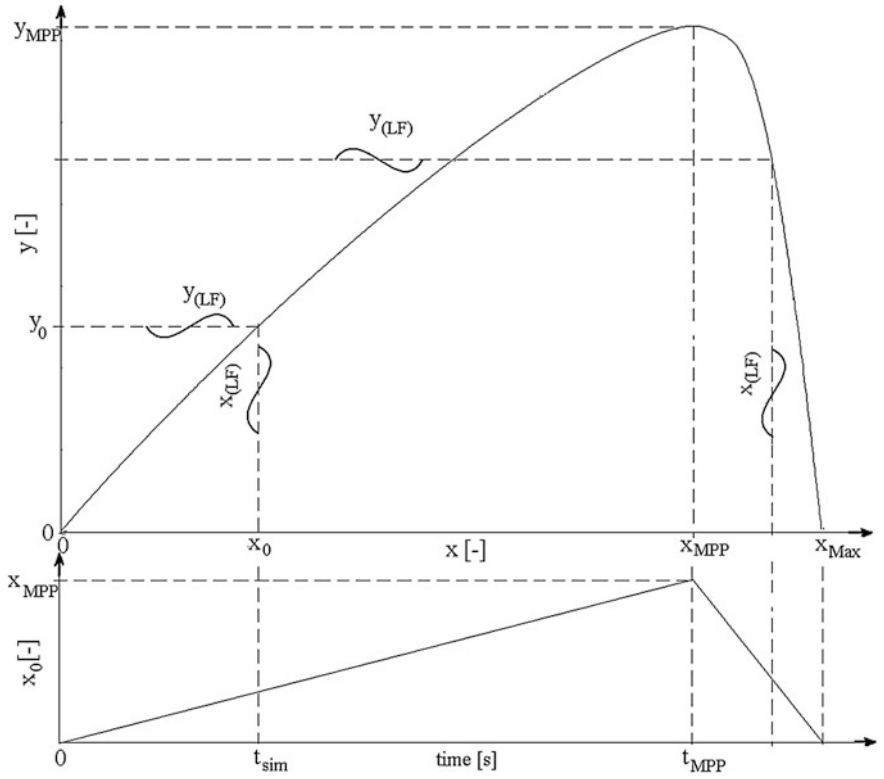

Fig. 12.2 Searching of the MPP based on dither signal ESC scheme [25]

model the nonlinear behavior of the PV system related to solar irradiance level. The PV power profile has multiple extremes due to the partially shading conditions. The temperature is also a very important parameter that affects the PV power, so a 2-D model may be used for the PV system using the irradiance and temperature as input variables. Also, the 2-D model for Proton Exchange Membrane (PEM) FC system (which is also known as Polymer Electrolyte Membrane FC system) will use the oxygen and hydrogen fueling flow rates. The GMPPT algorithm must track the GMPP between the multiple local extremes based on an ESC 2D-scheme, but this case will not be approached here.

A huge number of MPPT and GMPP algorithms have been developed in the last decades [6, 7], which are classified as offline, online and hybrid algorithms [6] or as conventional, computational, and soft computing techniques [7]. It is obvious that these MPPT and GMPP algorithms may be easily applied to harvest energy from all types of energy sources such as WT [8] and Fuel Cell (FC) stacks [9]. In this chapter the analysis of the MPPT and GMPP algorithms applied to FCHPS is shown.

The most know MPPT algorithms are the Perturb and Observe (P&O) [10], the Incremental Conductance (IC) [11] and the Hill Climbing (HC) [12] based on fixed or variable small searching steps to accurately track the MPP, but with limited searching speed because these performance indicators require opposite design values for the searching steps. Thus, if the step-size is increased to obtain a higher searching speed, then the tracking accuracy will be lower and vice versa.

Therefore, the advanced ESC schemes for the MPPT algorithms are usually proposed here to solve this problem and make less dependent the tracking accuracy to model used [5].

The group of soft computing techniques includes Artificial Intelligence (AI) algorithms such as the Fuzzy Logic Controller (FLC) [13], Artificial Neural Network (ANN) [14] and Evolutionary Algorithms (EA) [15]. As it was mentioned before, these AI-based MPP tracking algorithms are used to optimize the GMPP localization [15] in the first stage of searching, level of tracking oscillations [16] in second stage of searching or during the tracking phase, and control robustness [17].

Real-time optimization techniques such as the Ripple Correlation Control (RCC) [18] and ESC [19] schemes may increase the performance of searching of the GMPP. These GMPPT algorithms are based on perturbed signal injected in the control loop, which is usually named dither, or on ripple that normally exists on the HPS over the power generated by the energy source, being concentrated in harmonics at multiples of the grid (the low frequencies (LF) ripple) and switching frequency (the high frequency (HF) ripple).

Because it is impossible to simultaneously obtain a high searching speed and a good tracking accuracy using classical ESC schemes (such the high order ESC scheme (hoESC) [20]), advanced ESC schemes were reported in literature [21, 22]. Two classes of ESC approaches are reported in the literature: perturbation-based [23] and model-based methods [24].

The performance of the 1-D ESC schemes will be analyzed here based on the Band Pass Filter ESC (bpfESC) scheme proposed in [25–27] to increase both searching speed and tracking accuracy indicators.

Hydrogen is recognized as a viable energy source because it is widely spread in the Universe, being the most abundant elements in the Universe. The hydrogen energy is converted to electrical energy via the PEMFC systems that supply the FCHPS. This FCHPS is potentially a green energy resource that has no territorial restrictions, a competitive price, and a life cycle which continues to increase each year. Because it still requires expensive investments for hydrogen production, it is important to extract as much energy as possible from the PEMFC stack in order to reduce the hydrogen consumption [28]. Consequently, the PEMFC systems must operate close to MPP or MEP. The FC efficiency is with about 5% lower than the highest efficiency obtained at the MEP [28]. The MPPT algorithms for FC stack are retrieved from the PV system experience, but, in comparison with the PV systems, the operating point of a FC stack depends by more parameters of each subsystems of the FC system [29, 30]. Hybridization of the FC system with a Storage Devices, such as batteries and ultracapacitors which can be mixed in an Energy Storage System (ESS), and/or use of some RESs may be an effective technology to

overcome the disadvantages of the FC-alone-powered source [31–33]. The energy harvesting techniques need a MPPT control of adaptive type to harvest all the energy available from the microbial FC stacks used to treat the wastewater [34].

The FC power characteristic can be modeled using analytical equations [29] or numerical approximations [35] based on the loading and fueling conditions, stoichiometric air-fuel ratio, temperature and other parameters, such as transfer coefficients, internal humidity level, and catalyst layer thickness. Note that the last parameters are not simple simply available if these are not specified in the data sheet. The temperature is considered constant for the simulations performed here because its variation is slower than that on loading and fueling conditions.

As it was mentioned before, the P&O algorithms are the most used MPPT algorithms used for FC system, too [10, 36]. The design of the MPPT algorithms must carefully consider the tradeoffs between performance indicators (the searching speed and tracking accuracy) and safety operation. The FC power ripple must be as small as possible to increase the harvested power and to reduce the mechanical and electrical stress of the PEMFC membrane [37]. The control robustness to load dynamic could be assured by the load following control combined with the MPPT algorithms based on the ESC schemes [38, 39]. Although the ESC-based MPPT control is a well-established algorithm [20, 40, 41], certain instability may appear when the control parameters vary more quickly than action elements (for example, the air compressor) in order to increase the overall FC system efficiency [42, 43]. So, an MPPT-based energy management to load dynamic is required for the fueling flow rates [44–47]. The MPPT control would be beneficial to operate the FC stack because the MEP is difficult to be tracked [48] and in some cases the power density is more required than the fuel efficiency [49, 50].

In this chapter, three real-time optimization algorithms based on ESC schemes are compared as performance under different operating conditions of the PEMFC system. The ESC has been successfully applied in different engineering applications [51], which include the FCHPSs [52, 53]. The tracking accuracy reported for the PV inverters is higher than 99.98% [54], but lower accuracy (<99%) is reported for the FC inverter [55, 56]. Note that the tracking accuracy is defined as, where PMPP is the FC power at the MPP and PFC is the average power effectively generated by the FC system operating under MPPT control.

The chapter is organized as follows. Section 12.2 presents the classical High-Order ESC (hoESC) and bpfESC schemes used in simulation. If the transfer function of the Band Pass Filter (BPF) from the bpfESC scheme is equivalent to the series combination of the High-Pass Filter (HPF) and Low-Pass Filter (LPF) filters from the hoESC scheme, then the hoESC and bpfESC schemes are functionally equivalent, too. This aspect is briefly shown in this section. Section 12.3 deals with signal processing in the loop of the bpfESC scheme. An analytical analysis in the frequency and time domain of the bpfESC scheme is presented in order to compare the searching speed for both ESC schemes. The simulation results based on generic input-output maps validate the analytical results obtained. Section 12.4 briefly presents briefly the issue of modeling and control of the PEMFC system. Section 12.5 reviews the classical ESC, mESC and aESC schemes applied for the

PEMFC system, highlighting the main topological differences. The performance obtained is shown in Sect. 12.6 using the mESC and aESC schemes for PEMFC system under constant fueling rate and dynamic load profile. Last Section concludes the paper.

12.2 The Equivalence of the hoESC and bpfESC Schemes

The ESC schemes scans the plant's input, x, based on the plant's output, y, so that $y = f(x)$ is maximized (see Fig. 12.2). The searching of the MPP ($y \rightarrow y_{MPP}$) is assured if the staring value, x_0, will be set in the region of the MPP attraction. The noise level (n) does not affect the searching process in the closing loop [25, 26].

The performance's analysis of the hoESC (Fig. 12.3) and bpfESC (Fig. 12.4) schemes is performed in this section. It can be observed that both ESC schemes have the same operating relationships, excepting the signal filtering and demodulation [20, 24–26].

For brevity, only relationships of the bpfESC scheme are shown below, considering $G_{BPF}(s) = G_{HPF}(s) \cdot G_{LPF}(s) = [Y_{BPF}(s)/Y_F(s)] \cdot [Y_F(s)/Y_N(s)] = [s/(s + \omega_h)] \cdot [\omega_l/(s + \omega_l)]$:

$$y = f(x), y_{out} = y + n, y_N = k_N \cdot y_{out} \tag{12.1}$$

$$\begin{aligned} \dot{y_F} &= -\omega_h y_F + \omega_h y_N, y_{BPF} = y_N - y_F, \\ \dot{y_{BPF}} &= -\omega_l y_{BPF} + \omega_l y_F, y_{DM} = y_{BPF} \cdot \sin(\omega_d t) \end{aligned} \tag{12.2}$$

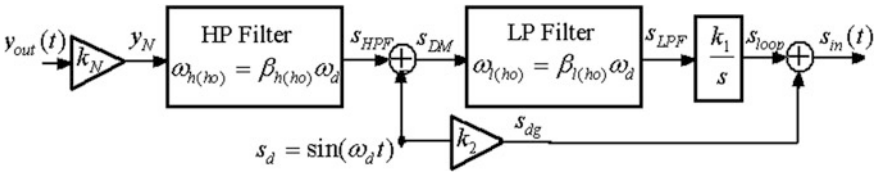

Fig. 12.3 The hoESC scheme [25]

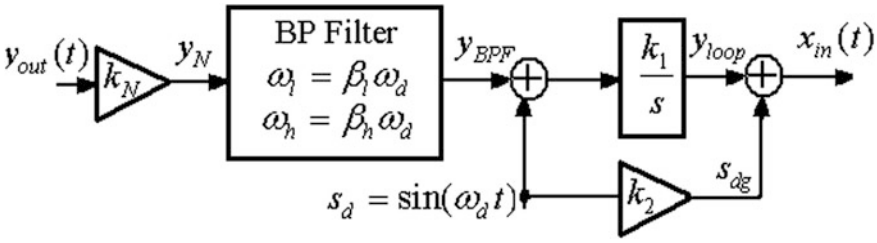

Fig. 12.4 The bpfESC scheme [25]

$$\dot{y_{loop}} = k_1 y_{DM} \tag{12.3}$$

$$x \cong x_{in} + x_0, x_{in} = y_{loop} + s_{dg}, s_{dg} = k_2 \cdot \sin(\omega_d t) \tag{12.4}$$

where Eqs. (12.1), (12.3), and (12.4) represent the input-to-output map, the integrator, the MPP current controller based on x_{in} reference, and Eq. (12.2) represent the signal processing based on BPF and demodulation.

The following notations are used (see Fig. 12.4):

- k_1 is the loop gain;
- k_2 is the gain of the dither amplitude;
- ω_d is the frequency of the dither signal;
- $\omega_l = \beta_l \omega_d$, $0 < \beta_l < 6$, is the cut-off frequency of the LPF;
- $\omega_h = \beta_h \omega_d$, $0 < \beta_h < 1$, is the cut-off frequency of the HPF;
- y_N is the signal after normalization (to the maximum value of y, y_{MPP});
- y_F is an intermediate variable related to HPF operating;
- y_{BPF} is the output signal from the BPF;
- y_{DM} is the signal after demodulation;
- y_{loop} is the output signal from the ESC loop;
- x_{in} is the estimation signal of the unknown parameter;

Relationships of the hoESC scheme related to signal processing based on LPF and HPF and demodulation are:

$$\begin{aligned} \dot{s_F} &= -\omega_h s_F + \omega_h s_N, s_{HPF} = s_N - s_F, \\ \dot{s_{LPF}} &= -\omega_l s_{LPF} + \omega_l s_{HPF} \sin(\omega t) \end{aligned} \tag{12.2'}$$

where s_N, s_{HPF}, and s_{LPF} are the signals after normalization, HPF, and LPF.

If $G_{BPF}(s) = G_{HPF(ho)}(s) \cdot G_{LPF(ho)}(s)$, then:

$$\begin{aligned} |G_{BPF}(\omega)| &= \left|G_{HPF(ho)}(\omega)\right| \left|G_{LPF(ho)}(\omega)\right|, \\ \phi_{BPF(ho)}(\omega) &= \arg(G_{BPF(ho)}) = \phi_{HPF(ho)}(\omega) + \phi_{LPF(ho)}(\omega) \end{aligned} \tag{12.5}$$

where:

$$\begin{aligned} \left|G_{HPF(ho)}(\omega)\right| &= 1/\sqrt{1 + \left(\omega_{h(ho)}/\omega\right)^2}, \\ \phi_{HPF(ho)}(\omega) &= \arg(G_{HPF(ho)}) = \arctan\left((\beta_{h(ho)}\omega_d)/\omega\right) \end{aligned} \tag{12.6}$$

$$\begin{aligned} \left|G_{LPF(ho)}(\omega)\right| &= 1/\sqrt{\left(\omega/\omega_{l(ho)}\right)^2 + 1}\,, \\ \phi_{LPF(ho)}(\omega) &= \arg(G_{LPF(ho)}) = -\arctan\left(\omega/(\beta_{l(ho)}\omega_d)\right) \end{aligned} \tag{12.7}$$

In this case, it was shown in [25] that the ratio of the searching speeds ($K_{SS(bpf)}$ and $K_{SS(ho)}$, respectively) is:

$$R_{SS} = \left|K_{SS(bpf)}/K_{SS(ho)}\right| = \left|\cos(\phi_{HPF(ho)} + \phi_{LPF(ho)})\right| / \cos(\phi_{HPF(ho)}) \tag{12.8}$$

If

$$0 < \beta_{h(ho)} < 1 < 3 < \beta_{l(ho)} \tag{12.9}$$

then

$$1 < R_{SS} \leq 1/\cos(\phi_{HPF(ho)}) \leq 1.0541 \tag{12.10}$$

the equality being obtained when:

$$\phi_{HPF(ho)} = \left|\phi_{LPF(ho)}\right| \Leftrightarrow \beta_{l(ho)} \cdot \beta_{h(ho)} = 1 \tag{12.11}$$

Thus, if $G_{BPF}(s) = G_{HPF(ho)}(s) \cdot G_{LPF(ho)}(s)$, then the hoESC (Fig. 12.3) and the bpfESC (Fig. 12.4) schemes will have almost the same search speed. So, from this point of view, the hoESC and the bpfESC schemes are functionally equivalent. It was shown in [25, 26] that almost the same tracking accuracy is obtained.

Relationship (12.11) also defines the condition to have the highest value of the search speed, $K_{SS(bpf)}$. It is important to know how much the search speed is improved for the bpfESC schemes, $K_{SS(bpf)}$, in comparison with hoESC scheme, $K_{SS(ho)}$.

If identical HPFs will be considered in both bpfESC and hoESC schemes, which means identical cut-off frequencies:

$$0 < \beta_{h(ho)} = \beta_{h(bpf)} < 1 \tag{12.12}$$

then the ratio of the searching speeds ($K_{SS(bpf)}$ and $K_{SS(ho)}$, respectively) is:

$$R_{SS} = \left|K_{SS(bpf)}/K_{SS(ho)}\right| \cong \left|G_{LPF(bpf)}\right| / \left|G_{LPF(ho)}\right| \tag{12.13}$$

If

$$0 < \beta_{l(ho)} < 1 < 3 < \beta_{l(bpf)} \tag{12.14}$$

then

$$\left(\beta_{l(bpf)}/\sqrt{\beta_{l(bpf)}^2 + 1}\right) \geq 0.95 \tag{12.15}$$

Thus, the following average approximation can be used [24]:

$$R_{SS} \cong \sqrt{1 + 1/\beta_{I(ho)}^2} \tag{12.16}$$

In the next section a better approximation will be developed based on the signal processing in the bpfESC loop.

12.3 The Signal Processing in the ESC Loop

The probing signal related to the input-output map, y = f(x), can be approximated by the Taylor series:

$$y(x) = \sum_{i=0}^{\infty} \frac{(x - x_0)^i}{i!} \cdot \frac{d^i f}{dx^i}(x_0) \tag{12.17}$$

where (x_0, $y_0 = f(x_0)$) is a point on the static power map, which slowly varies in time as it is shown in Fig. 12.1. If the starting point is considered the origin, (0, 0), then the ramp for $t < t_{MPP}$ is given by relationship:

$$x_0(t) = \frac{x_{MPP}}{t_{MPP}} \cdot t = G \cdot t \tag{12.18}$$

Note that t_{MPP} is the time of simulation and G is the slope of the ramp used to test the nonlinear plant in open loop or it is the gradient that is estimated in closed loop, K_{SS}.

In both cases, the derivatives can be computed during the simulation based on relationship:

$$\frac{df}{dx}(x_0) = \frac{df}{dt} \Big/ \frac{dx}{dt} \cong G^{-1} \cdot f^{(1)}(t) \tag{12.19}$$

In general:

$$\frac{d^i f}{dx^i}(x_0) \cong G^{-i} \frac{d^i f}{dt^i}(t) = G^{-i} f^{(i)}(t) \tag{12.20}$$

The main LF components in the ESC loop are set by the frequencies band of the BPF or equivalent series connection of the HPF and LPF:

$$x_{LF}(t) = \sum_{j=1}^{[\beta_I]} a_j \sin(j\omega_d t) \tag{12.21}$$

where the integer $[\beta_l]$ can be set higher than 3 to increase the ration of searching speeds.

The magnitudes of the LF components, a_j, are lower than the x_0 value, so:

$$x = x_0 + x_{LF} \cong x_0 \tag{12.22}$$

and

$$\frac{dx}{dt} \cong \frac{dx_0}{dt} \tag{12.23}$$

Consequently:

$$y_{BPF}(t) \cong k_N \sum_{i=1}^{\infty} \left\{ \left[\sum_{j=1}^{[\beta_l]} a_j \sin(j\omega_d t) \right]^i \frac{G^{-i} f^{(i)}(t)}{i!} \right\} \tag{12.24}$$

12.3.1 Estimation of the Searching Speed in the bpfESC Loop

The estimation of the searching speed in the bpfESC closed loop will be performed considering the following assumptions:

- only three components of the Taylor series will be considered;
- the BPF is ideal, having $\beta_{h(bpf)} = 0.5$ and $\beta_{l(bpf)} = 3.5$;
- $G = 1$ and $k_N = 1$.

Under these conditions the relationship (12.24) will become:

$$y_{BPF}(t) \cong \sum_{i=1}^{3} \left\{ \left[\sum_{j=1}^{3} a_j \sin(j\omega_d t) \right]^i \frac{f^{(i)}(t)}{i!} \right\} \tag{12.25}$$

If the superposition technique will be considered, then the relation (12.25) will be written as:

$$y_{BPF}(t) \cong \sum_{i=1}^{3} \left\{ \left[\sum_{j=1}^{3} a_j^i \sin^i(j\omega_d t) \right] \frac{f^{(i)}(t)}{i!} \right\} \tag{12.26}$$

The signal after the demodulation

$$y_{DM}(t) = y_{BPF}(t) \cdot \sin(\omega_d t) \tag{12.27}$$

can be written as:

$$y_{DM}(t) \cong K_{sg} + \sum_{j=1}^{3} \left[b_j \sin(j\omega_d t) + c_j \cos(j\omega_d t) \right] \tag{12.28}$$

where:

$$K_{sg} = \frac{f^{(1)}(t) \cdot a_1}{2} + \frac{f^{(3)}(t) \cdot a_1^3}{16} \tag{12.29}$$

and

$$\begin{aligned}
b_1 &= \frac{f^{(2)}(t) \cdot a_1^2}{8}, \\
c_1 &= \frac{f^{(1)}(t) \cdot a_2}{2} + \frac{f^{(3)}(t) \cdot a_2^3}{16}, \\
b_2 &= 0, \\
c_2 &= \frac{f^{(1)}(t) \cdot (a_1 - a_3)}{2} + \frac{f^{(3)}(t) \cdot \left(4 \cdot a_1^3 - 3 \cdot a_3^3\right)}{48}, \\
b_3 &= \frac{f^{(2)}(t) \cdot \left(a_2^2 - a_1^2\right)}{8}, \\
c_3 &= -\frac{f^{(1)}(t) \cdot a_2}{2} - \frac{f^{(3)}(t) \cdot a_2^3}{16}
\end{aligned} \tag{12.30}$$

The K_{sg} parameter will be computed in simulation based on the next relationship:

$$K_{sg} = \frac{a_1}{2} \cdot \frac{df}{dx}(x_0) + \frac{a_1^3}{16} \cdot \frac{d^3 f}{dx^3}(x_0) \tag{12.29'}$$

Relationships (12.30) can be used to estimate the harmonics magnitudes in the bpfESC open loop, but to accurately compute these magnitudes in the closed loop these relationships must be rewritten considering the derivatives as above.

The signal injected in the loop will be:

$$y_{loop}(t) = k_1 \int y_{DM}(t)dt \cong k_1 K_{sg} \cdot t + \sum_{j=1}^{3} \left[\frac{k_1 c_j}{j\omega_d} \sin(j\omega_d t) - \frac{k_1 b_j}{j\omega_d} \cos(j\omega_d t) \right] \tag{12.31}$$

The loop gain, k_1, is set proportional to the dither frequency in order to assure the dither persistence in the ESC loop [25, 26]. So, if

$$k_1 = \gamma_{sd} \cdot \omega_d \tag{12.32}$$

then

$$y_{loop}(t) \cong K_{SS(bpf)} \cdot t + \sum_{j=1}^{3} \left[H_j \sin(j\omega_d t + \varphi_j) \right] \tag{12.33}$$

where $K_{SS(bpf)}$ and H_j are the values estimated in the closed loop for the searching speed and the magnitude of the j-harmonic:

$$\begin{aligned} K_{SS(bpf)} &= K_{sg} \cdot \gamma_{sd} \cdot \omega_d \\ H_j &= \frac{\gamma_{sd}}{j} \cdot \sqrt{b_j^2 + c_j^2} \end{aligned} \tag{12.34}$$

Note that these parameters are time variables based on relationships (12.29) and (12.30).

12.3.2 Estimation of the Searching Speed in the hoESC Loop

The estimation of the searching speed in the hoESC closed loop will be performed considering the same assumptions as in the section above, excepting that $\beta_{h(ho)} = 1.5$.

The LF components in the hoESC loop are filtered by the LPF, thus only the first harmonic will be considered:

$$x_{LF}(t) = a_1 \sin(\omega_d t) \tag{12.35}$$

The signal after the HPF is:

$$s_{HPF}(t) \cong a_1 \frac{df}{dx}(x_0) \cdot \sin(\omega_d t) \tag{12.36}$$

Thus, the signal after demodulation can be written as:

$$\begin{aligned} s_{DM}(t) &= s_{HPF}(t) \cdot \sin(\omega_d t) \cong a_1 f^{(1)} \cdot \sin^2(\omega_d t) \\ &= a_1 f^{(1)}/2 - a_1 f^{(1)} \cdot \cos(2\omega_d t)/2 \end{aligned} \tag{12.37}$$

Consequently, the signal after the LPF will be:

$$s_{LPF}(t) \cong a_1 f^{(1)}/2 \tag{12.38}$$

so:

$$s_{loop}(t) = k_1 \int s_{LPF}(t)dt \cong \left(k_1 a_1 f^{(1)}/2\right) \cdot t = K_{SS(ho)} \cdot t \tag{12.39}$$

where:

$$K_{SS(ho)} = k_1 a_1 f^{(1)}/2 = \gamma_{sd}\omega_d \frac{a_1}{2} \cdot \frac{df}{dx}(x_0) \tag{12.40}$$

12.3.3 Estimation of the Speeds' Ratio During the Searching Phase

The ratio of the searching speeds can be estimated based on relationship (12.35) and (12.40) as below:

$$R_{SS}(t) = \frac{K_{SS(bpf)}}{K_{SS(ho)}} = 1 + \left|\frac{df^3}{dx^3}(x_0)/\frac{df}{dx}(x_0)\right| \cdot \frac{H_1^2(t)}{8} \tag{12.41}$$

where the magnitude of the first harmonic, H_1, for the y_{BPF} signals will be estimated using the Fast Fourier Transform (FFT). The diagram shown in Fig. 12.5 is implemented in Matlab-Simulink® and used for comparative tests for the hoESC and bpfESC schemes operating in closed loop, considering different input-output maps such as:

$$y_p = f_p(x) = 1 - (1 - x)^{2p}, p = 1, 2, 3 \tag{12.42}$$

The computing block (see Fig. 12.5) estimates the ratio of the searching speeds based on (12.41).

12.3.4 Simulation Results

The following parameters are used for the bpfESC schemes in all simulations: $\gamma_{sd} = 0.2$ ($k_1 = 2\pi\gamma_{sd}f_d$), $\beta_{h(bpf)} = 0.18$ and $\beta_{l(bpf)} = 5.5$. Besides these, two values are used for the dither frequency (f_d) and for the gain of the dither magnitude (k_2) to highlight some analytical results using the simulation performed. The used values for the dither are mentioned in each case.

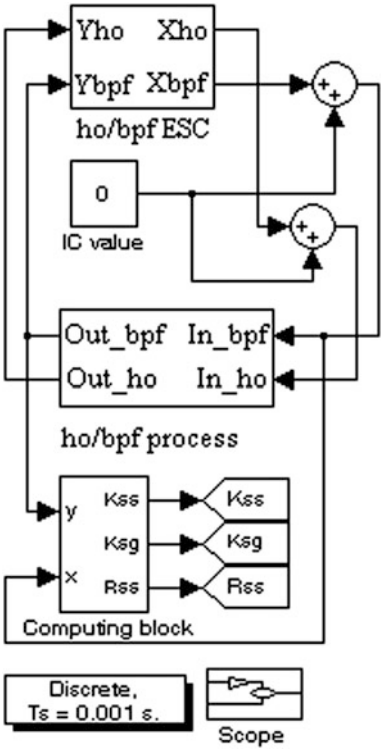

Fig. 12.5 The diagram for performance's comparison of the hoESC and bpfESC schemes [25]

The derivatives for the input-output maps considered, $y_p = f_p(x) = 1 - (1 - x)^{2p}$, p = 1, 2, 3, are:

$$\begin{aligned} y_p^{(1)}(x_0) &= \frac{df}{dx}(x_0) = 2p(1-x_0)^{2p-1}, p = 1,2,3 \\ y_p^{(3)}(x_0) &= \frac{d^3f}{dx^3}(x_0) = 2p(2p-1)(2p-2)(1-x_0)^{2p-3}, p = 2,3 \\ y_1^{(3)}(x_0) &= 0, p = 1 \end{aligned} \tag{12.43}$$

These relationships (12.43), above mentioned, were implemented in the computing block for both ESC schemes.

The simulations presented in Fig. 12.6 related to the searching phase for the hoESC (●) and bpfESC (■) schemes, using f_d = 50 Hz (case a), and f_d = 5 Hz

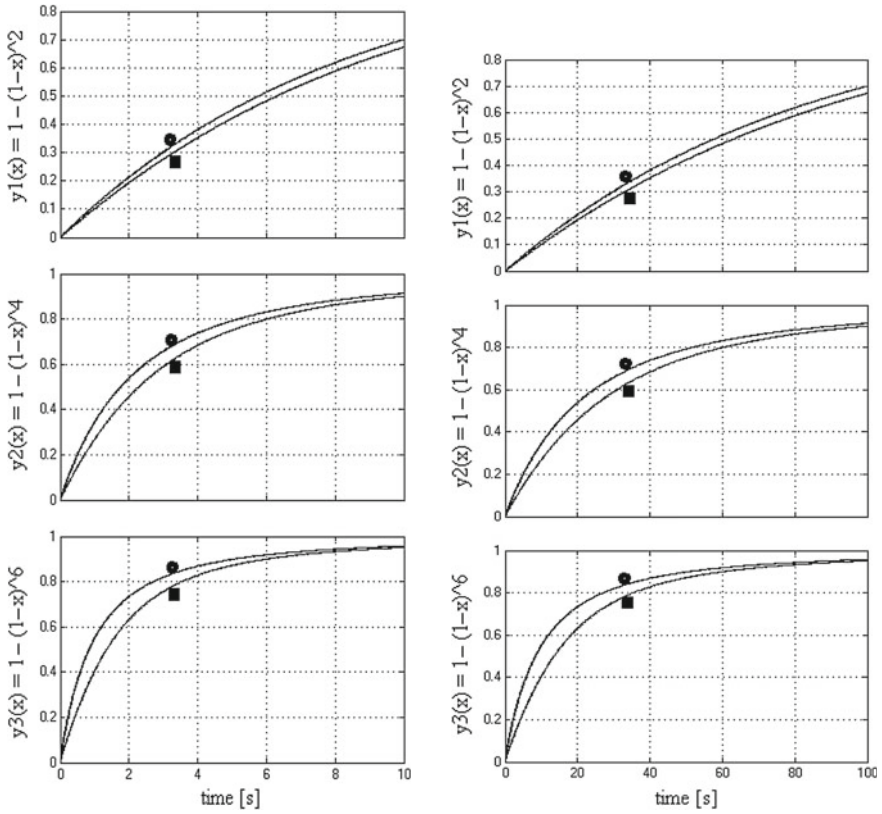

(a) f_d=50 Hz **(b)** f_d=5 Hz

Fig. 12.6 The search phase for the hoESC (●) and bpfESC (■) schemes with γsd = 0.2 ($k_1 = 2\pi fd$), k_2 = 0.001, βl(ho) = 1.5, βh(bpf) = 0.18 and βl(bpf) = 5.5 [25]

(case b), shown that the number of iterations (or dither's periods) is almost the same for each ESC scheme.

Based on the zooms shown in Fig. 12.7 at t = 0.2 s (case a), and t = 2 s (case b), the ratio of the searching speeds can be estimated for each input-output maps, $y_p = f_p(x)$, as being about 1, 1.3, and 1.8 for p = 1, 2, and 3, respectively. The average value computed based on (12.16) is 1.2 and 2.2, for the $\beta_{l(ho)}$ value of 1.5 and 0.5, respectively.

The searching speeds are computed based on (12.34) and (12.29') and the simulation results are shown in Fig. 12.8 for the same cases and parameters

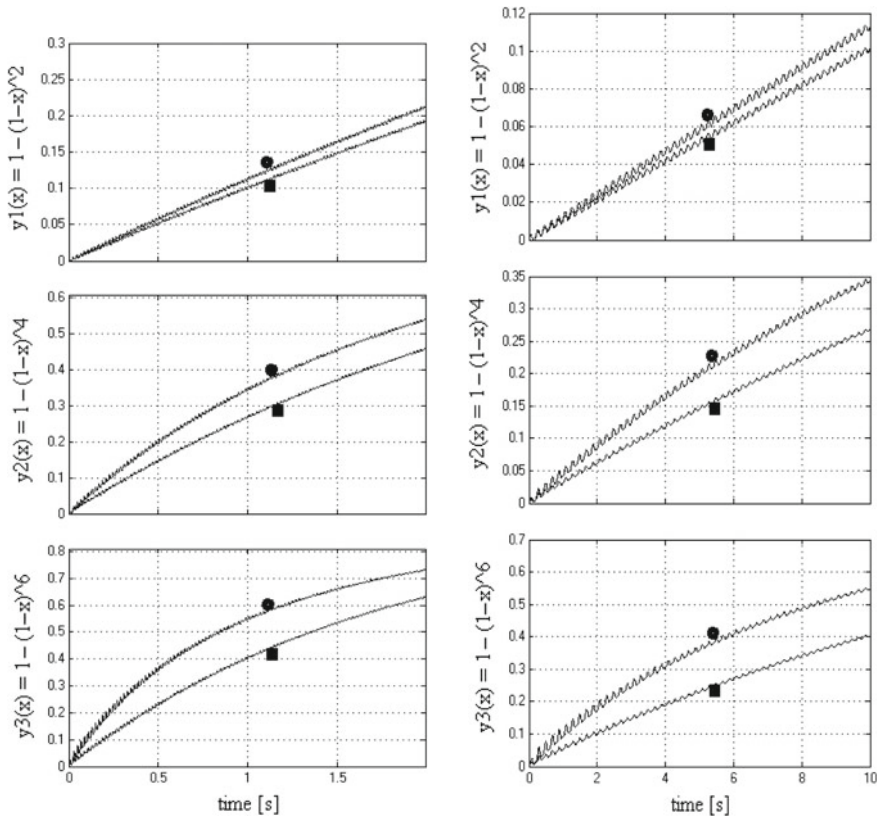

(a) f_d=50 Hz **(b)** f_d=5 Hz

Fig. 12.7 Zooms of the search phase for the hoESC (●) and bpfESC (■) schemes with γsd = 0.2 ($k_1 = 2\pi\gamma sdfd$), k_2 = 0.001, βl(ho) = 1.5, βh(bpf) = 0.18 and βl(bpf) = 5.5 [25]

mentioned above. The simulation results shown in Fig. 12.8 validate the analytical results presented above for the bpfESC scheme:

- The shape of the $K_{SS(bpf)}$ (top), $K_{sg(bpf)}$ (middle) and H_1 (bottom) during the search phase is the same (see Fig. 12.8).
- The average value of the $K_{sg(bpf)}$ (middle) and H_1 (bottom) is almost the same for both frequencies.
- The initial value for the $K_{sg(bpf)}$ parameter is about 0.07 (for p = 3) and 0.018 (for p = 2) in both cases. Also, the initial value for the H_1 magnitude is about 0.024 (for p = 3) and 0.09 (for p = 2) in both cases. On the other hand, considering the above comments and the value of $a_1 = H_1$, the initial value for the $K_{sg(bpf)}$ parameter can be estimated based on (12.29') as:

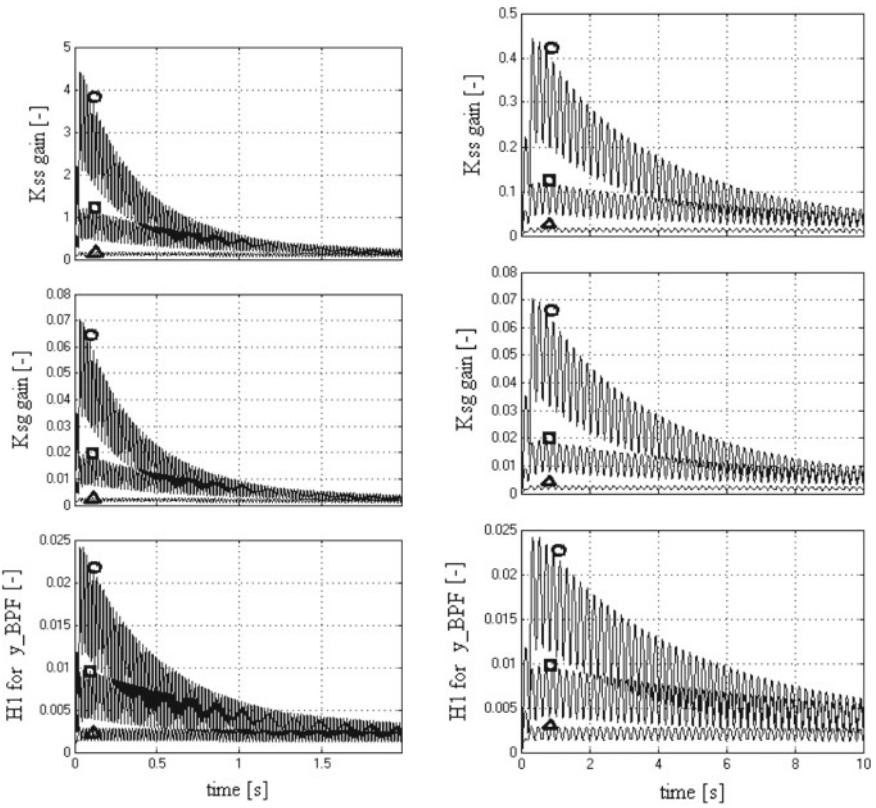

Fig. 12.8 KSS(bpf) (*top*), Ksg(bpf) (*middle*) and H_1 (*bottom*) during the searching phase for the bpfESC scheme with γsd = 0.2 ($k_1 = 2\pi\gamma sdfd$), k_2 = 0.001, βh(bpf) = 0.18 and βl(bpf) = 5.5, and different input-output map: yp = 1 – (1 – x)2p, p = 1 (●), 2 (□), and 3 (△) [25]

$$K_{sg}(0) \cong \frac{a_1}{2} \cdot \frac{df}{dx}(0) = p \cdot H_1,\ p = 1, 2, 3 \tag{12.44}$$

It is easy to notice that the above simulation results validate the relationship (12.44). For example, considering γ_{sd} = 0.2 and f_d = 50 Hz (case a), the initial value for the $K_{SS(bpf)}$ indicator is about 0.7 (for p = 3) and 0.18 (for p = 2). Thus, considering the initial value for the simulated $K_{sg(bpf)}$ parameter mentioned above, the γ_{sd} parameter can be estimated based on (12.34) as 4.4/(314 · 0.07) ≅ 0.2 (for p = 3) and 1.2/(314 · 0.018) ≅ 0.21 (for p = 2).

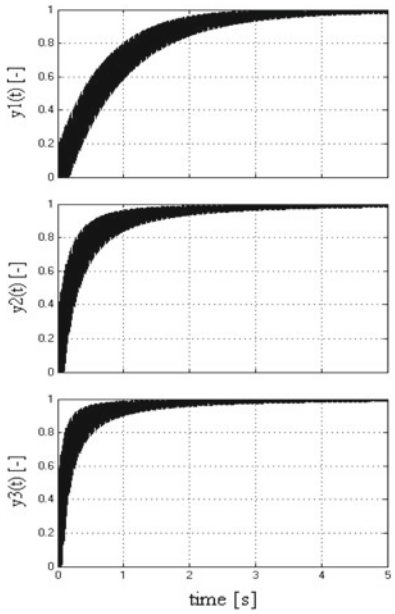

(a) The output during the searching phase for different input-output map, $y_p=1-(1-x)^{2p}$, p=1 (top), 2 (middle), 3 (bottom)

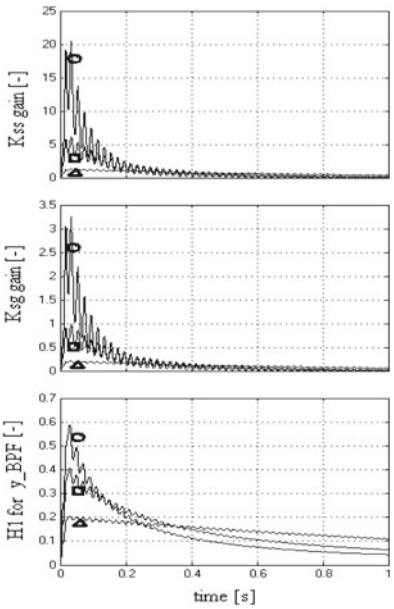

(b) $K_{SS(bpf)}$ (top), $K_{sg(bpf)}$ (middle) and H_1 (bottom) for different input-output map: $y_p=1-(1-x)^{2p}$, p=1 (●), 2 (□), 3 (△)

Fig. 12.9 The bpfESC scheme with $\gamma sd = 0.02$ ($k_1 = 2\pi\gamma sdfd$), $k_2 = 0.1$, fd = 50 Hz, $\beta h(bpf) = 0.18$ and $\beta l(bpf) = 5.5$ [25]

Also, it is easy to notice that the values for the $K_{SS(bpf)}$ indicator are 10-times lower in case b, when the dither frequency is set to be 10-times lower than in case a. Thus, the analytical result given by (12.34), related to the $K_{SS(bpf)}$ indicator, is validated through simulation.

In order to highlight the second term of the relationship (12.29'), some simulations related to the searching phase for the bpfESC schemes using $k_2 = 0.1$, which is 100-times higher than the above value, are presented in Fig. 12.9. To assure the loop stability the k_1 gain is set 10-times lower than the above value considering in simulation $\gamma_{sd} = 0.02$ and $f_d = 50$ Hz.

The simulation results validate the analytical results presented above for the bpfESC scheme:

- The convergence time is proportional to the product of the frequency and magnitude of the dither. The convergence time is 10-times lower in Fig. 12.10 than in Fig. 12.7a.
- Considering the initial value for the $K_{SS(bpf)}$ indicator and $K_{sg(bpf)}$ parameter, the γ_{sd} parameter can be estimated based on (12.34) as $20/(314 \cdot 3) \cong 0.021$ (for p = 3) and $6/(314 \cdot 0.9) \cong 0.021$ (for p = 2). Thus, the analytical result given by (12.34) is further validated through simulation.

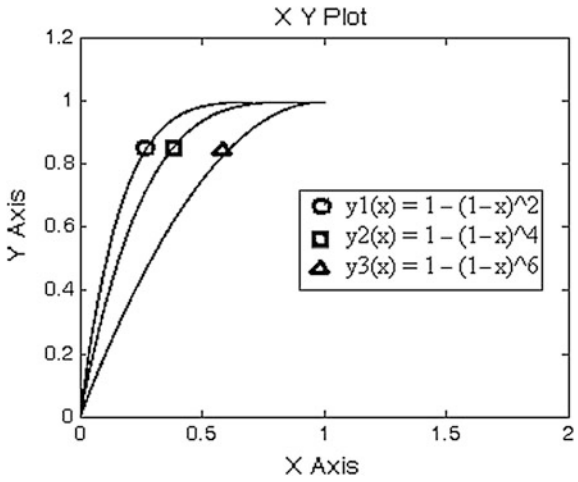

Fig. 12.10 The search phase is shown in the Y-X phase plane for yp = 1 – (1 – x)2p: p = 1(○), 2(□), 3(△) [25]

The searching phase is shown in the Y-X phase plane for different $y_p = 1-(1-x)^{2p}$ is shown in Fig. 12.10.

The ratios of the searching speeds can be estimated based on (12.41) for the mESC and bpfESC scheme using $y_p = 1 - (1 - x)^{2p}$, and these value are validated by the simulations shown in Fig. 12.11.

The simulation results validate the analytical results obtained based on (12.43):

- Case p = 3: the initial ratio of the searching speed is $1 + (120/6) \cdot (0.6)^3/8 = 1.9$; the initial ratio computed from the simulation results is about 2.
- Case p = 2: the initial ratio of the searching speed is $1 + (24/4) \cdot (0.4)^3/8 = 1.12$; the initial ratio computed from the simulation results is about 1.14.

Note that the dither has a higher magnitude during the search phase (see bottom plot in Fig. 12.8b). The ripple during the stationary phase is shown in Fig. 12.12.

The ripple measured during the stationary phase (around t = 4 s) is about 3.5% (for p = 1), 2.5% (for p = 2), 2% (for p = 3). For example, if a FC stack has 10 kW power, then the power ripple is higher than 200 W, which means a lot from energy efficiency point of view of energy efficiency. Furthermore, the ripple affects the life cycle of the PEMFC stack. As it was mentioned, a solution to improve the tracking accuracy was proposed in [26].

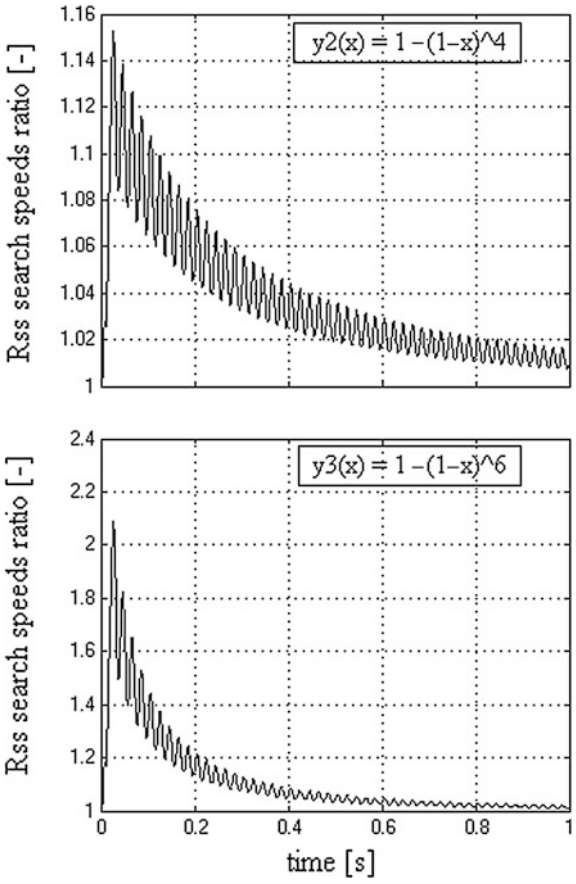

Fig. 12.11 The ratio of the searching speeds for the mESC and bpfESC scheme (with γsd = 0.02, k_2 = 0.1, fd = 50 Hz, βh(bpf) = 0.18 and βl(bpf) = 5.5) using $y_p = f(x) = 1 - (1 - x)2p$: p = 2 (*top*), 3(*bottom*) [25]

12.4 FC System Modeling and Control

12.4.1 FC System Modeling

The PEMFC system converts the hydrogen energy into electrical energy. Besides other FC types, the PEMFC system has some advantages in operating such as low operating temperature, compactness, and more simplified procedures to start-up and shut-down.

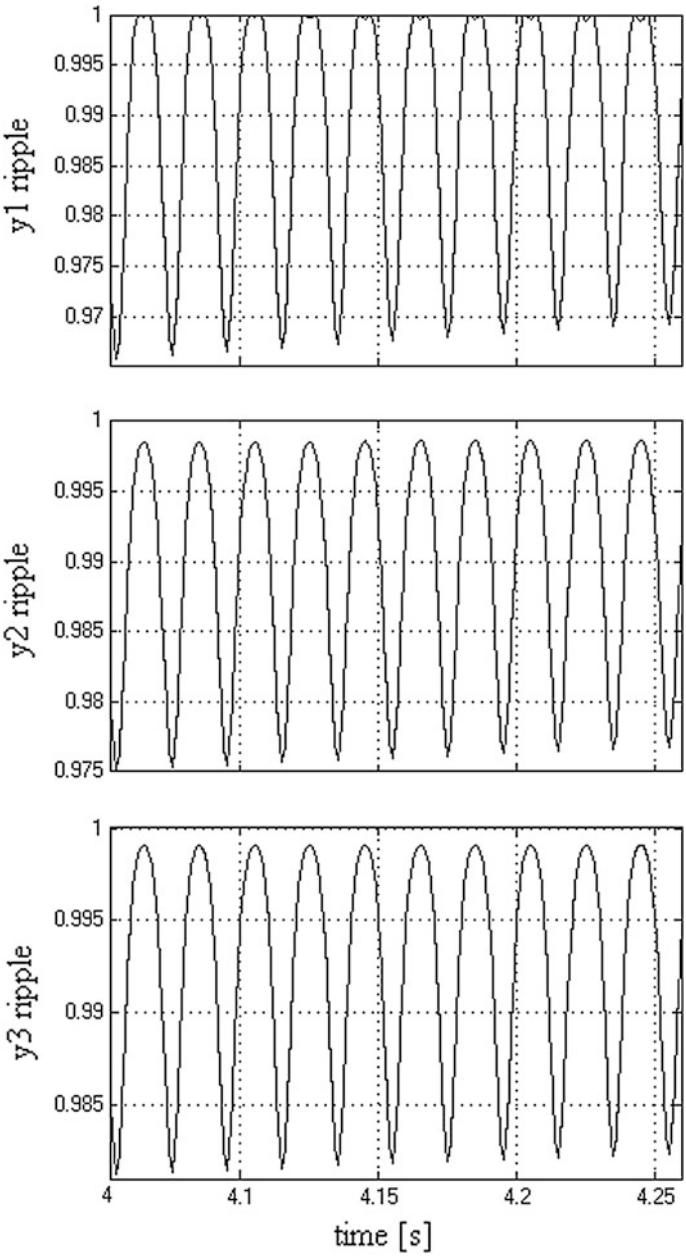

Fig. 12.12 Ripple during the stationary phase for the bpfESC scheme with $\gamma sd = 0.02$ ($k_1 = 2\pi\gamma sdfd$), $k_2 = 0.1$, fd = 50 Hz, $\beta l(bpf) = 0.18$, $\beta h(bpf) = 5.5$, and $y_p = 1 - (1 - x)2p$: p = 1(*top*), 2(*middle*), 3(*bottom*) [25]

The model used for the FC system should be able to accurately reflect the PEMFC fueling and loading, the mass transfer and electrochemical phenomena, which have time constants that must be included into the PEMFC dynamic. The analytical models are focused on different processes encountered on the FC system such as heat, mass transfer, electrochemical phenomena and other [57], or on entire system [58, 59]. The empirical models are based on experimental data and focused to predict the effect of different input parameters on the FC power, without in-depth analysis of the physical and electrochemical phenomena involved [35, 60].

The PEMFC model implemented in Matlab/Simulink® will be used here because this model has good accuracy in reflecting the PEMFC operation. The model accuracy is not a critical issue: the ESC-based MPPT algorithm will track the MPP of the FC power characteristic that is simulated at 3380 K (because the effects of temperature are negligible on MPP position during the tracking process).

The hydrogen consumption is proportional to the FC current. The MPP controller will regulate the FC current to maximize the FC power by controlling the fueling rate [42, 47]. The humidified air flow is regulated by the air controller, which commands the compressor's speed for the required FC power [42]. The classical control of the air flow rate is based on maintaining the oxygen excess ratio close to 2 [57]. Both fuel flow rates can be used to control the FC power [47], but for high FCHPS the air control is usually used [42, 60], without maximization of the FC system efficiency [61].

It is obvious that the FC power could be controlled by both fueling rates or only by air flow rate [62, 63], this choose being in general an experimental challenge for the FCHPS designers [64–67]. Anyway, a model for the FCHPS is necessary to design the fueling controller. In general, a nine or five states variables are used to model the PEMFC system (named full-order model [63, 65] or reduced model [66, 67], respectively).

12.4.2 FC System Control

12.4.2.1 Air Flow Control

The air flow rate must be efficiently controlled based on the load following controller. If the air flow rate is higher that the needed rate then the efficiency of the PEMFC system decreases, but also if this decreases under the needed rate, close to critical rate, then the air is insufficient and the oxygen starvation may appear. The controlled compressor can regulate the cathode excess oxygen ratio, avoiding this phenomenon. The air rate may be controlled using a dynamic feed-forward control,

linear quadratic regulator, robust control, predictive control, sliding control, MPPT control and so on [18, 43, 63, 67, 68]. Here, the ESC-based MPPT control will be analyzed.

12.4.2.2 Hydrogen Flow Control

The hydrogen flow rate can directly regulate the FC power, respecting the stoichiometric ratio of hydrogen and oxygen flow rates and dynamic range of the mass flow controllers. The hydrogen flow rate is a very good manageable variable, instead of the oxygen flow rates that is a poor manipulated variable to control the FC power [62–64]. The optimal hydrogen flow rate is estimated in real-time based on the PEMFC efficiency map [69]. This control is benefic for small PEMFC systems, where it is impractical to recycle the unreacted hydrogen [50].

The FC power will fall after few FC time constants after the shutdown of the fuel valve and the FC power returns to the previous value if the fuel valve is reopened during this delay in powering (when the reactants in the manifolds are not consumed) [62]. So, the control of the on-off fuel valve must be made at a switching frequency lower than 0.5 Hz. Thus, this control of the FC power is impractical due to the slow response of the control loop. Consequently, a linear controlled valve is used to regulate the pressure of hydrogen [50] or oxygen [45]. The control loop is more complex, containing a valve, flowmeter, and an appropriate controller. A simple and cheap control loop may be obtained using a digital valve, which is a set of carefully sized sonic chokes installed in parallel (supplied by one common inlet line and all discharged into a common exit manifold). The chokes calibrated and sized in a binary pattern flowing may be digitally controlled using the on-off fuel valves in series with each choke. A digital approximation is obtained for the hydrogen flow rate that may be designed to be close to those given by the linear controlled valve.

12.4.2.3 Control of Both Fueling Flow Rates

The control objective is to maximize the net FC power based on the both fueling rates that are controlled in the admissible 2-D domain specified by the constraints. In this case, a 2D-scheme for controlling both fueling flows can be used [21, 47, 70]. In general, a large tracking accuracy error is obtained due to the weak controllability of the fueling flow rates under pulsed load [71]. The modeling and the control of the air stream and hydrogen flow with recirculation in a PEMFC system with constraints is shown in [66, 72]. The ESC 2D-scheme to control both fueling

flows is analyzed in [47]. Here, the proposed mESC scheme of single input single output type will be analyzed to highlight its advantages in comparison with the classical control schemes.

12.5 The ESC-Based MPPT Control for FC System

The objective of the ESC scheme is to generate the control reference (Iref) that generates the FC output power close to PMPP without knowing the FC power characteristic, PFC = f(IFC). Consequently, the current control mode based on the ESC-based MPPT control will be implemented to regulate the fuel flow rate (FuelFr) using the following load technique [26, 39].

12.5.1 The Classical ESC Schemes

The first order ESC scheme is based on a scalar scheme, which is as that represented in Fig. 12.3, but without use of the filters' blocks [73].

The hoESC scheme is augmented with filters of LPF and HPF type, as in Fig. 12.3 [25] or adapted for the FC system in Fig. 12.13 [26], where the dither gain is $k_A = A \cdot k_2$. Note that the LPF is not always necessary in searching and tracking of the MPP, excepting the noise environment [52].

12.5.2 The mESC Scheme

The mESC scheme was shown in Fig. 12.3 [25] and adapted to the FC system in Fig. 12.14 [26], where the dither gain is $k_A = A \cdot k_2$. The initial value of the FC current, I_{FC0}, must be set in the attraction region that assures $i_5 \rightarrow I_{MPP}$.

The analysis performed in next sections for the ESC schemes is based on a sinusoidal dither, but the dithers' shape does not influence the performance [74].

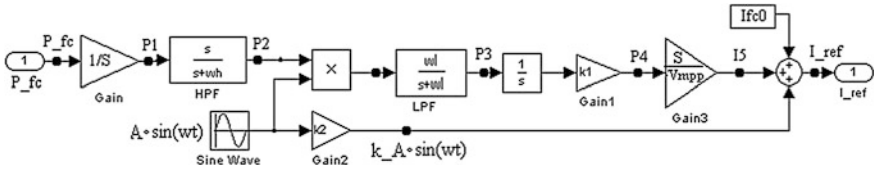

Fig. 12.13 The hoESC scheme for FC system [26]

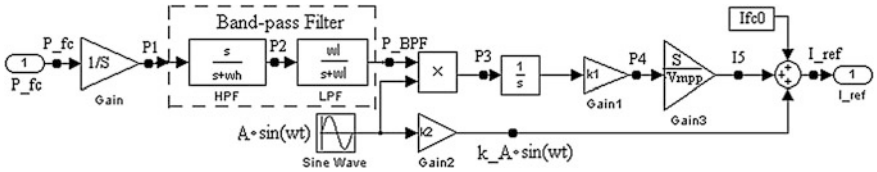

Fig. 12.14 The mESC scheme for FC system [26]

12.5.3 The aESC Scheme

The aESC scheme is shown in Fig. 12.15 [27]. Note that the dither amplitude is set to be proportional with the first harmonic's magnitude (H_1) of the FC power: Thus, the dither gain is $k_A = A \cdot k_2 \cdot H_1$. The first harmonic's magnitude (H_1) decreases during the searching process to almost zero at MPP. Consequently, an insignificant ripple of FC power will be on FC bus during the stationary phase. The proposed aESC scheme outperforms the classical ESC schemes and the mESC scheme in global power efficiency if the search speed is limited to be the same for all ESC schemes.

Note that aESC scheme will have the same operating relationships as mESC scheme (1–4), excepting that dither gain is $k_A = A \cdot k_2 \cdot H_1$.

The equivalent aESC (EQaESC) scheme that uses a series connection of HPF and LPF, instead of a BPF, is also shown in Fig. 12.15. The aESC and EQaESC schemes are functionally equivalent if the filters have the same cut-off frequencies. So, the performance of both aESC and EQaESC schemes are almost the same. The demonstration can be made in the same manner as in Sect. 12.2 for hoESC and bpfESC schemes.

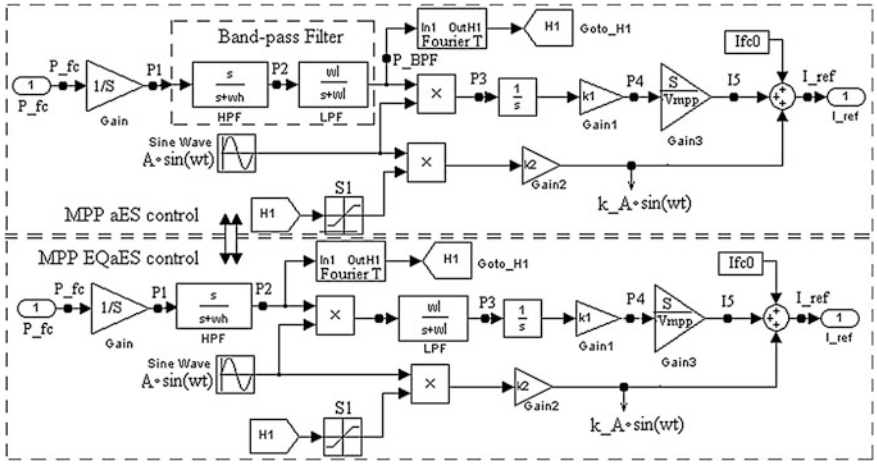

Fig. 12.15 The aESC scheme and its equivalent scheme (EQaESC) [27]

12.6 Testing of the ESC Schemes on PEMFC System

12.6.1 Testing at Constant Fueling Rate

The Matlab-Simulink® diagram shown in Fig. 12.16 contains the 6 kW–45 V PEMFC stack system that has the fueling rate set by the FuelFr constant and the FC current controlled by the ESC-based MPP controller.

The preset PEMFC model has the nominal flow rates for hydrogen and air of 50 and 300 lpm, membrane aria (S) of about 65 cm^2, 65 cells in series (resulting the voltage at light load, $V_{FC(0)}$, of about 60 V), and the MPP will be around 129 A (I_{MPP}) and 6175 W (P_{MPP}). The PEMFC characteristic shown in Fig. 12.17 is obtained for the nominal fueling conditions mentioned in this figure, too. The PEMFC time constant was set in range 0.2–2 s and the dither frequency in the range 1–100 Hz in order to analyze the dynamic effects.

The MPPT process is represented in the P-I phases plane (see Figs. 12.17 and 12.18). The dither's gain (k_2) and dither's frequency modifies the magnitude and position of the limit cycle (see Fig. 12.17). This means that the power ripple remains constant during the stationary phase (see the zoom on Fig. 12.18). The power ripple decreases to zero during the stationary phase if the aESC scheme is used. This aESC scheme will be analyzed in Sect. 12.6.4, highlighting its performance in comparison with mESC scheme.

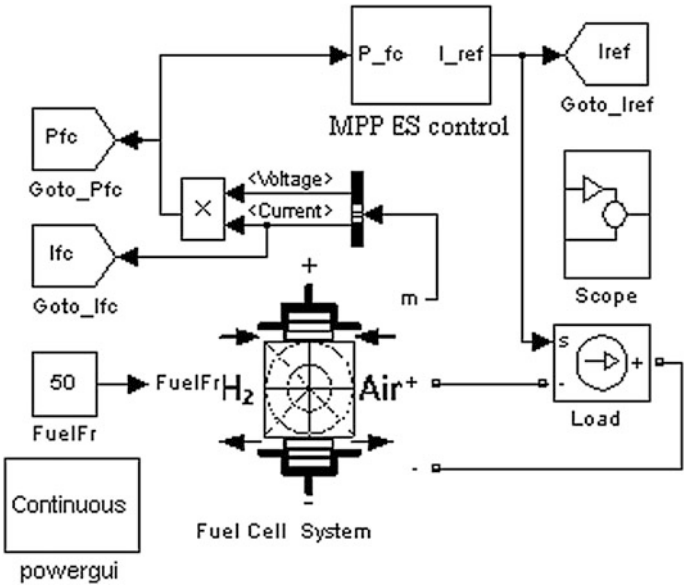

Fig. 12.16 Diagram for testing the ESC schemes [26]

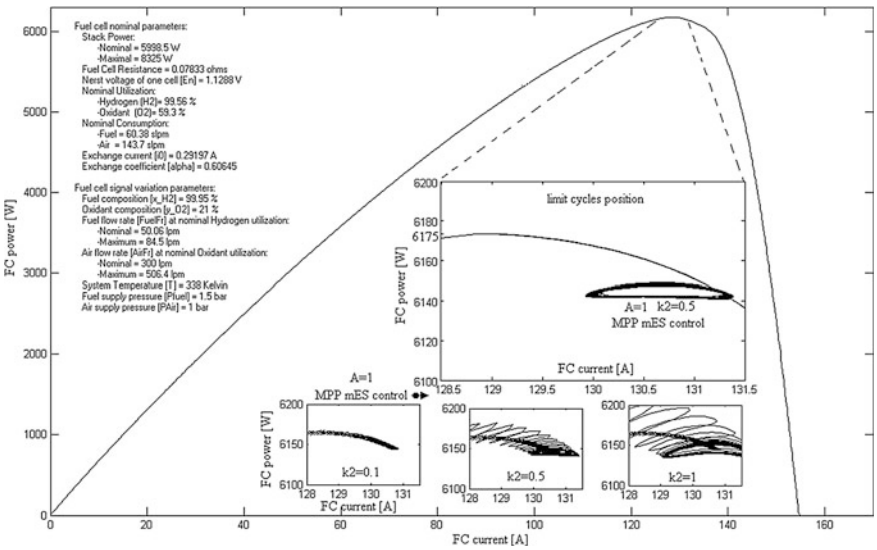

Fig. 12.17 The FC power characteristics versus the FC current, and the MPP position close to limit cycle obtained for the mESC scheme [26]

The harmonics' magnitudes for three level of the FC power are also shown in Fig. 12.17. The magnitude (H_1) of the first harmonic decreases during the searching phase, being almost zero close to the MPP. In this section the performance of the mESC scheme in comparison with the EQmESC and the hoESC scheme will be shown using the diagram from Fig. 12.19. The FC system without MPP control is used as reference

The fuel flow rate, FuelFr (lpm), is computed based on the load current, i_L (see Fig. 12.20):

$$FuelFr = \frac{60000 \cdot R \cdot (273 + \theta) \cdot N_C \cdot (i_L \cdot G_i)}{2F \cdot (101325 \cdot P_f) \cdot (U_{f(H2)}/100) \cdot (x_{H2}/100)} \tag{12.45}$$

where:

R = 8.3145 J/(mol K);
F = 96485 A s/mol;
N_C represents the number of cells in series (65);
$U_{f(H2)}$—nominal hydrogen utilization (99.56%);
θ—operating temperature (65 °C);
P_f—fuel pressure (1.5 bar);
x_{H2}—H_2 composition (99.95%);
$G_i = I_{FC}/I_L$.

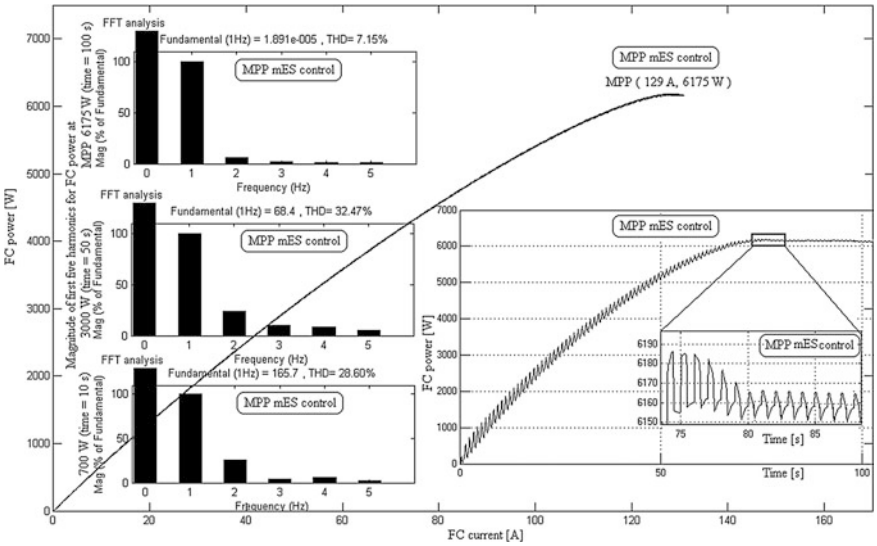

Fig. 12.18 The MPP tracking on the P-I phases plane for the mESC scheme (a zoom of the tracking accuracy is included) [26]

The G_i gain will be used to set the charge-sustained regime for the ESS [39]. Here, $G_i = 1$ in all simulations, so it was omitted in Fig. 12.20. The rate limiter with saturation of the FuelFr value assures safe operation for the PEMFC system.

12.6.2 The Equivalence of the mESC and EQmESC Schemes for FC System

The LF equivalence (EQ) of the hoESC and bpfESC schemes was theoretically approached in Sect. 12.2 of this chapter. Some simulations to validate this theoretical result were shown in Sect. 12.3.4 and will be shown here for the mESC and EQmESC schemes adapted from the hoESC and bpfESC schemes (see Figs. 12.2, 12.3, 12.13 and 12.14, respectively) for a FC system. The simulation results are shown in Fig. 12.21. The FC system behavior under the mESC and EQmESC schemes is almost the same (see the profile of the FC power and the LF harmonics of the i_{ref}). The simulation parameters for the both mESC and EQmESC schemes are the following: $k_1 = 400$, $k_A = A \cdot k_2 = 0.1$ ($k_2 = 1$, and $A = 0.1$), $f_d = \omega_d/(2\pi) = 100$ Hz, $\beta_l = 5.5$, and $\beta_h = 0.5$ (thus $\beta_l \cdot \beta_h = 2.75$). The fuel flow rate is nominal (50 lpm). A saw-tooth load is used for the FC system without MPP control in order to estimate the tracking accuracy (see the top zoom on right part of Fig. 12.21). Also, the zooms on the left part of Fig. 12.21 are obtained for $\beta_l = 5.5$

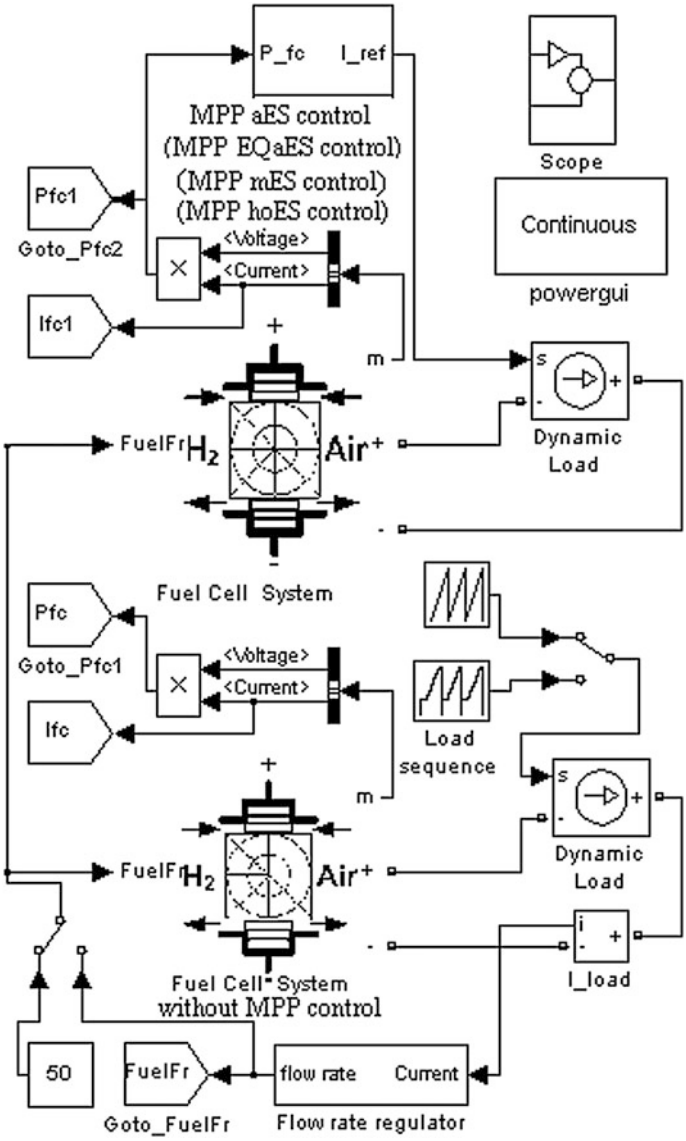

Fig. 12.19 The diagram for comparative tests for different ESCschemes analyzed [25]

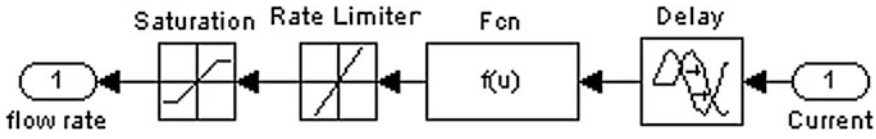

Fig. 12.20 The diagram of the flow rate regulator [26]

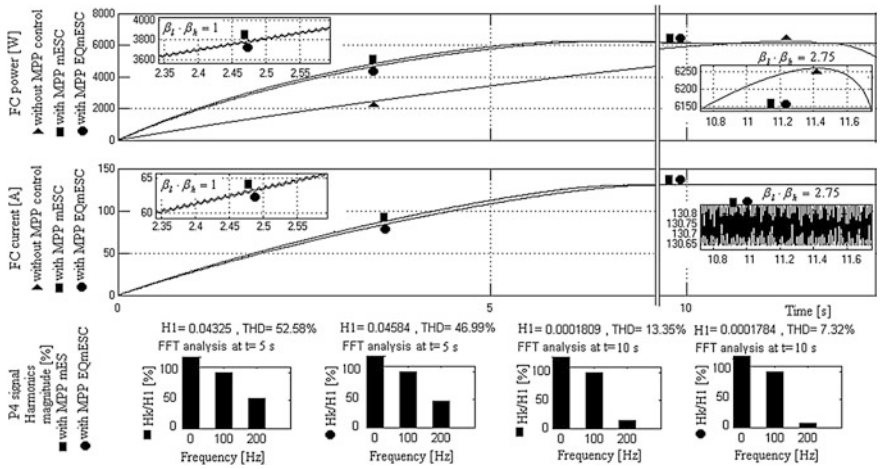

Fig. 12.21 Simulation results for the mESC and EQmESC schemes [26]

and $\beta_h = 1/\beta_l \cong 0.18$ (because $\beta_h \cdot \beta_l = 1$) and highlights the validity of the relationship (12.11) during the search time phase: $\beta_l \cdot \beta_h = 1$.

Thus, the simulation results have again validated the analytical results reported in Sect. 12.2. The main performances of the mESC scheme based on the results shown in Fig. 12.21 are the following:

- The oscillations of the FC current is about 0.2 A peak-to-peak, being obtained if the dither period (10 ms) is chosen lower than the FC time constant (2 s).
- The power ripple is about 9 W (0.2 A · 45 V) for $k_A = 0.1$, and the normalized power ripple is about 9/6000 = 1.5%, being on admissible range mentioned in [55].
- The tracking accuracy is 6150/6250 ≅ 0.984 = 98.4% (see Fig. 12.21), being lower than 99% of the value reported in [56];
- The both mESC and EQmESC schemes have almost the same searching speed. For example, the initial search rate of the FC current is about 30 A/s, so the power increases with a rate of 1800 W/s, which is verified on the FC power shown on the top of Fig. 12.21.

12.6.3 The Performance of the mESC and hoESC Schemes for FC System

The ratio of the searching speeds for mESC and hoESC schemes is given by (12.46):

$$R_{SS} \cong \sqrt{1 + 1/\beta_{l(ho)}^2} \tag{12.46}$$

where the approximation was made because

$$\left(\beta_{l(bpf)}/\sqrt{\beta_{l(bpf)}^2 + 1}\right) \geq 0.95 \quad \text{for} \quad 0 < \beta_{l(ho)} < 1 < 3 < \beta_{l(bpf)}.$$

The simulations shown in Fig. 12.22 validate again the relationship (12.16). All parameters used in simulation were set the same for both mESC and hoESC schemes ($k_1 = 400$, $k_2 = 1$, $A = 0.1$, $f_d = \omega_d/(2\pi) = 100$ Hz, and $\beta_h = 0.5$), with the exception of the cut-off frequency of the filters ($\beta_{l(m)} = 5.5$ and $\beta_{l(ho)} = 0.5$).

The comparison of the performance obtained for both ESC schemes is as following:

- The searching speeds for both mESC and hoESC schemes are time dependent variable. For example, the speeds' rates evaluated at 2 s are about 1500 Ws^{-1} and 1000 Ws^{-1} for the mESC and hoESC schemes, respectively. The speeds' ratio is 2.2 based on (12.16), being higher than the ratio evaluated based on the simulation results (which is 1500/1000 = 1.5) due to the harmonics effects explained in Sect. 12.3.
- The searching speed is proportional to the dither magnitude based on relationship (12.35) and (12.40). This results are validated by the results shown in Fig. 12.22 (see zoom on left of Fig. 12.22) for $k_2 = 1$ and $A = 1$. The searching speed is about ten time higher for both ESC schemes if the dither amplitude is 10 times higher than the value $A = 0.1$, which was mentioned above.

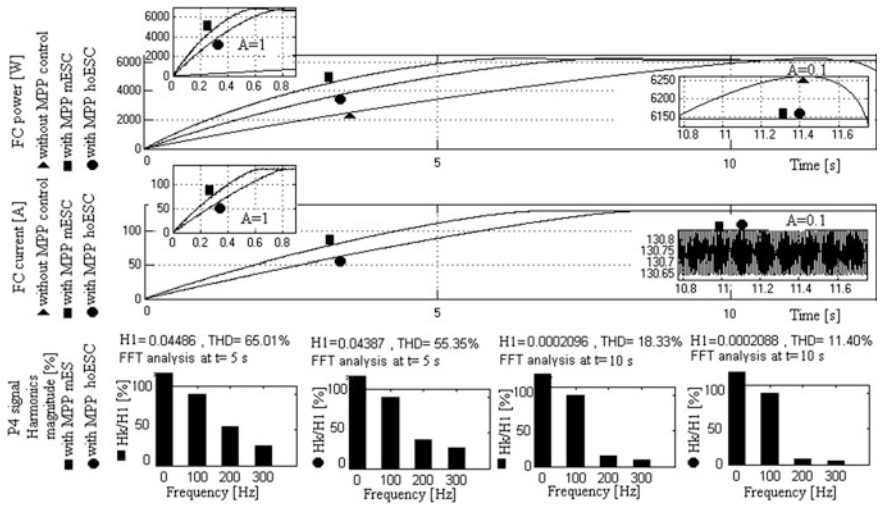

Fig. 12.22 Simulation results for the mESC and hoESC schemes [26]

- The LF harmonics content of the i_5 control signal is different for the ESC schemes (see the spectrums shown on bottom of the Fig. 12.22) due to different values used for the cut-off frequencies: $0 < \beta_{l(ho)} < 1 < 3 < \beta_{l(bpf)}$. For example, the magnitude of second harmonic is with about 30% higher, so the dither's persistence on the mESC loop is better than that resulting on the hoESC loop.
- The design of the k_1 gain to be proportional to the dither frequency will assure certain dither's persistence on the mESC loop, which will guarantee the convergence of the ESC algorithm.

12.6.4 The Comparative Analysis of the aESC and mESC Schemes

As it was mentioned above, the main difference between the mESC scheme and the aESC scheme is related to the dither gain, which is constant, $k_{A(m)} = A \cdot k_2$, and time variable, $k_{A(a)} = A \cdot k_2 \cdot H_1$, respectively, where H_1 is the magnitude of first harmonic of the FC power.

Consequently, the searching speed for the aESC and the mESC schemes are given by (12.46) and (12.47) [25, 26]:

$$\begin{aligned} K_{SS(i)(aES)} &= K_{SS(p)(aES)}/V_{MPP} \\ &= \dot{p_{FC}}\, k_{1(a)} k_{2(a)} A \left| G_{BPF(a)} \right| \cos(\phi_{BPF(a)})/(2V_{MPP}) \end{aligned} \tag{12.46}$$

$$\begin{aligned} K_{SS(i)(mES)} &= K_{SS(p)(mES)}/V_{MPP} \\ &= \dot{p_{FC}}\, k_{1(m)} k_{2(m)} H_1 A \left| G_{BPF(m)} \right| \cos(\phi_{BPF(m)})/(2V_{MPP}) \end{aligned} \tag{12.47}$$

If the same design parameters will be used for the aESC and mESC schemes ($k_{1(a)} = k_{1(m)}$ and $k_{2(a)} = k_{2(m)}$ and so on), then the ratio of searching speeds will be:

$$R_{SS} = \left| K_{SS(aESC)}/K_{SS(mESC)} \right| \cong H_1 \tag{12.48}$$

If the same filters are used, $BPF_{(a)} \equiv BPF_{(m)}$, and the S1 saturation block has the limits 0 and 1, then $k_{A(a)} = k_{A(m)}$ during the searching phase (when $H_1 > 1$) and $k_{A(a)} = H_1 k_{A(m)}$ if the MPP was located and $H_1 < 1$. The H_1 magnitude is very small close to the MPP, so the FC power ripple is negligible during the stationary phase and the MPP is found accurately (see Fig. 12.23, where the magnitudes of the first three harmonics (H_1, H_2, and H_3) of the FC power are shown).

Note that the searching speed will be H_1—times higher for the aESC scheme in comparison with the mESC scheme if the S1 saturation block has the upper limit set to infinit. The rate limiter with saturation of the FuelFr value will assure the safe operation for the PEMFC system (see the flow rate regulator diagram in Fig. 12.23).

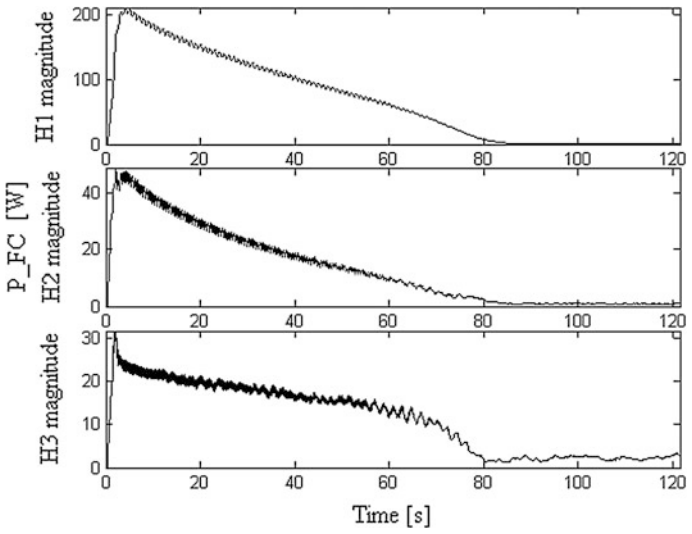

Fig. 12.23 The harmonics of the FC power [27]

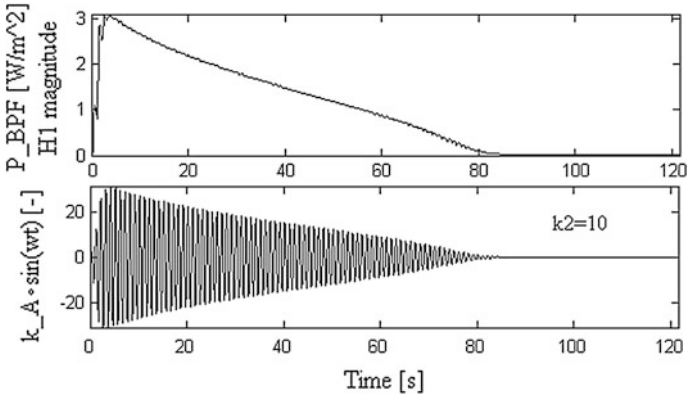

Fig. 12.24 The shape of the 100 Hz dither signal [27]

The FC power density (the ratio of the FC power to membrane aria), which is the p_1 signal in Fig. 12.15, is filtered by the BPF, resulting the p_{BPF} signal. This signal modulates the dither signal (with A = 1 and the dither gain $k_2 = 10$; see Fig. 12.24).

If the same k_1 gain ($k_{1(a)} = k_{1(m)}$) and filters ($BPF_{(a)} \equiv BPF_{(m)}$) are used, A = 1 and the S1 saturation block has the upper limit 0.5, then $k_{A(a)} = 0.5$ (because $H_1 > 1$) and $k_{A(m)} = k_2$ during the searching phase. See the searching speeds in the first column of zooms on Fig. 12.25, where the load sequence is stair step type and

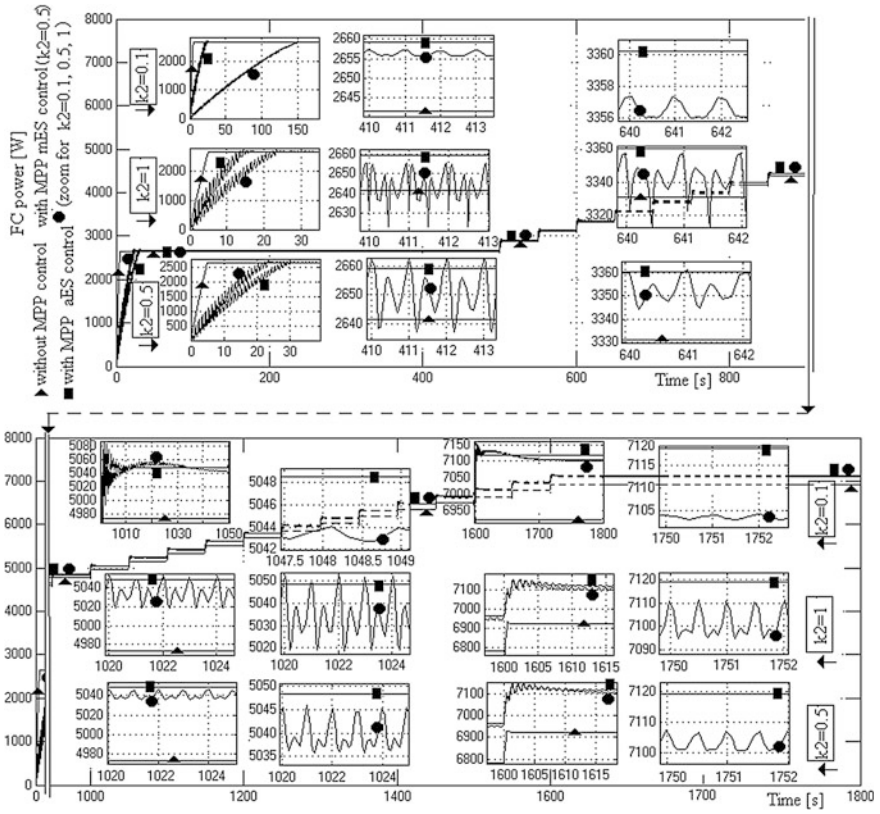

Fig. 12.25 The FC power using the aESC (■) and mESC (●) schemes, and without MPP control (▲); the zooms shown the details of MPP searching and tracking process [27]

three values are considered for the k_2 parameter: $k_2 = 0.5$, $k_2 = 1$, and $k_2 = 0.1$ for zooms shown on bottom, middle and top of Fig. 12.25.

The next columns of zooms show the MPP tracking process for the aESC (when $k_{A(a)} = H_1 k_{A(m)}$ because $H_1 < 1$ if the MPP was located) and mESC schemes. The tracking accuracy for aESC scheme is higher than that of the mESC scheme, which is 6160/6175 = 0.9976 = 99.76% at full load (see Fig. 12.18).

The comparative results highlight the advantages of the aESC scheme in comparison with the mESC scheme:

- the ratio of search speeds is $R_{SS} = \left| K_{SS(aESC)} / K_{SS(mESC)} \right| \cong H_1$;
- the MPP tracking accuracy is higher than 99.76% for the aESC scheme;
- the FC power ripple using the aESC scheme is negligible, but the FC power ripple using the mESC scheme is about 1 W, 10 W, and 20 W for k_2 parameter set to 0.1, 0.5, and 1, respectively.

12.6.5 Testing the aESC Scheme on FCHPS

The FCHPS is shown in Fig. 12.26, where an equivalent load is used to test the FCHPS. The design of the FCHPS is detailed in [27]. Here, only the results are shown to validate the performance of the aESC scheme. Two control loops can be identified in Fig. 12.26: the load following loop (with $G_i = 4$ set in relation (12.45)) and the aESC-based MPPT loop.

The results of the FCHPS behavior under aESC-based MPPT control are shown in Fig. 12.26 as following:

- Plot 1: the load power profile, including a zoom of load ripple and its power spectrum;
- Plot 2: the FC power (●) and the H_1 magnitude of the p_{BPF} signal (■);
- Plot 3: the FC current, including a zoom of the load ripple and its power spectrum.

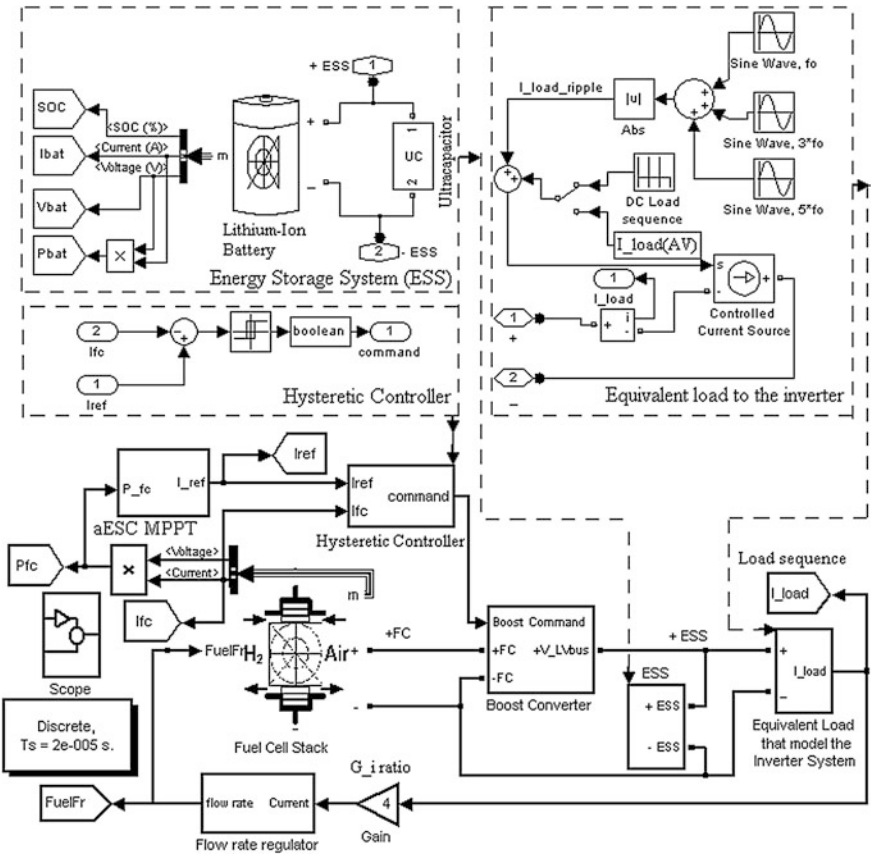

Fig. 12.26 The FCHPS diagram under aESC-based MPPT control [27]

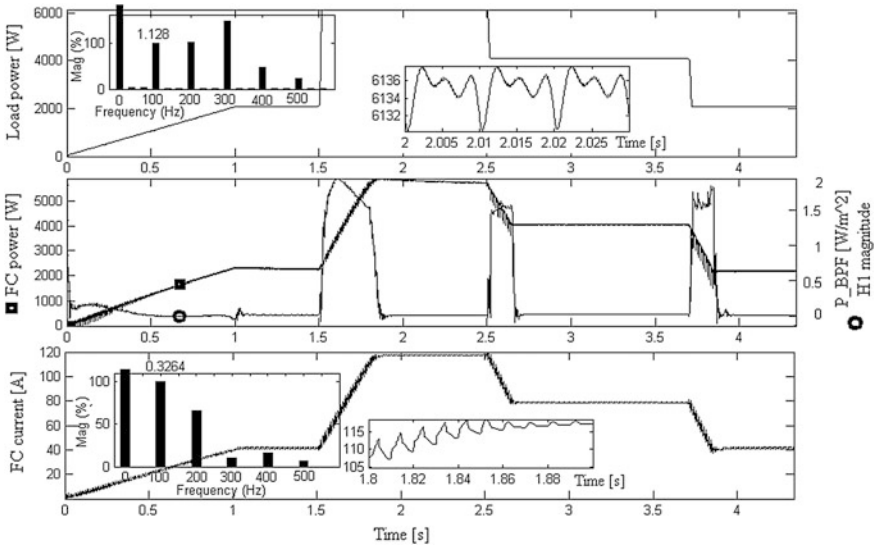

Fig. 12.27 The FCHPS behavior under aESC-based MPPT control [27]

The MPPT process can be understood based on the results shown in Fig. 12.27: the H_1 magnitude increases quickly at any load variation, which actually means a FC power that follows the load profile based on the load following control implemented.

The search speed is about a few kW/s (see plot 2 on Fig. 12.27).

The power flow balance on DC bus is assured by the ESS, which will operate in charge depletion mode load ($P_{load} > \eta_{boost} P_{FC} \Rightarrow P_{ESS} > 0$) or in the charge increasing mode ($P_{load} < \eta_{boost} P_{FC} \Rightarrow P_{ESS} < 0$).

12.7 Conclusion

In this chapter, besides the well-known results for the hoESC scheme, which are obviously available for the all ESC schemes, new analytical results related to the bpfESC scheme are shown. The main results are: (1) the searching speed may be estimated based on the derivatives of the unknown input-output map; (2) the harmonics magnitudes during the searching phase could be evaluated based on (12.34); (3) the ratio of the searching speeds can be estimated during the searching phase based on (12.41).

Note that these results related to ratio estimation must be interpreted in the context of the modeling approach considered, which was kept at a simple level for the signal processing in the ESC loop. All the analytical results obtained were validated by simulation using generic input-output maps. The FC power

characteristic was used as input-output map to validate the above results on this nonlinear map (see Sect. 12.6). The mean value of the searching speeds ratio was computed to shown that this is close to the average approximation of this ratio based on a frequency approach given by (12.13). Also, it can be noted that the dither persistence is dependent to the BPF cut-off frequencies.

The mESC scheme based on the bpfESC was proposed to improve the performance related to searching speed process. The main results of the comparison of the mESC scheme with the hoESC scheme are the following: (1) the rate of searching speeds is higher than 1.5 in all cases; (2) the dither's persistence is improved if the frequencies band of the BPF is enlarged; (3) the search speed could be set up to safe value by increasing the dither gain until the admissible value that is designed for an imposed performance for the tracking accuracy and the FC power ripple.

Note that the FC power ripple and tracking accuracy are almost the same for both ESC schemes analyzed. These performance indicators were improved by the aESC scheme that was analyzed in comparison with mESC scheme (see Sect. 12.6.4): (1) the tracking accuracy is higher than 99.76%, (2) the FC power ripple is negligible during the stationary phase after the MPP is found; (3) the search speed could be set up to safe value, but maintaining the performance related to the tracking accuracy and the FC power ripple; (4) the aESC-based MPPT control is robust to load profiles that include high dynamic variations; (5) the aESC-based MPPT control is simple to be implemented.

It was shown that the aESC scheme slightly outperforms the mESC scheme in total power efficiency and performance obtained for any load profile. The aESC searching speed is H_1 times higher than the mESC searching speed, which finally means a very short time to find and track the current MPP.

Thus, the aESC-based MPPT control combined with the load following control has good performance for nonlinear loads with unmodeled dynamics.

The performance of the FCHPS with two control loops that was highlighted in this chapter could influence the designers to experiment this control architecture.

Acknowledgements The research that led to the results shown here has received funding from the project "Cost-Efficient Data Collection for Smart Grid and Revenue Assurance (CERA-SG)", ID: 77594, 2016-19, ERA-Net Smart Grids Plus. Some figures, tables and text are reproduced from [25–27] here with kind permission from Elsevier Limited, UK, and IJTPE—IOCTPE, [February 13, 2016].

References

1. Dargahi M, Rouhi J, Rezanejad M, Shakeri M (2009) Maximum power point tracking for fuel cell in fuel cell/battery hybrid power systems. Eur J Sci Res 25(4):538–548
2. Esram T, Chapman PL (2007) Comparison of photovoltaic array maximum power point tracking techniques. IEEE Trans Energy Convers 22(2):439–449
3. Salas V, Olías E, Barrado A, Lázaro A (2006) Review of the maximum power point tracking algorithms for stand-alone photovoltaic systems. Sol Energy Mat Sol Cells 90(11):1555–1578

4. Caux S, Hankache W, Fadel M, Hissel D (2010) On-line fuzzy energy management for hybrid fuel cell systems. Int J Hydrogen Energy 35(5):2134–2143
5. Wang J-C, Su Y-L, Shieh J-C, Jiang J-A (2011) High-accuracy maximum power point estimation for photovoltaic arrays. Sol Energy Mat Sol Cells 95:843–851
6. Reisi AR, Moradi MH, Jamasb S (2013) Classification and comparison of maximum power point tracking techniques for photovoltaic system: a review. Renew Sust Energy Rev 19:433–443
7. Ishaque K, Salam Z (2013) A review of maximum power point tracking techniques of PV system for uniform insolation and partial shading condition. Renew Sust Energy Rev 19:475–488
8. Dali M, Belhadj J, Roboam X (2010) Hybrid solar-wind system with battery storage operating in grid–connected and standalone mode: control and energy management—experimental investigation. Energy 35(6):2587–2595
9. Khanh LN, Seo JJ, Kim YS, Won DJ (2010) Power-management strategies for a grid-connected PV-FC hybrid system. IEEE Trans Energy Convers 25(3):1874–1882
10. Giustiniani A et al (2010) Enhancing polymeric electrolyte membrane fuel cell control by means of the perturb and observe technique. Fuel Cell Sci Technol 7(1):11021–11031
11. Liu F, Duan S, Liu F, Liu B, Kang Y (2008) A variable step size INC MPPT method for PV systems. IEEE Trans Ind Electron 55(7):2622–2628
12. Xiao W, Elnosh A, Khadkikar V, Zeineldin H (2011) Overview of maximum power point tracking technologies for photovoltaic power systems. In: 37th annual conference of IEEE IES 2011. IECON 2011, pp 3900–3905
13. Bouchafaa F, Hamzaoui I, Hadjammar A (2011) Fuzzy logic control for the tracking of maximum power point of a PV system. Energy Procedia 6:633–642
14. Karlis AD, Kottas TL, Boutalis YS (2007) A novel maximum power point tracking method for PV systems using fuzzy cognitive networks (FCN). Electr Power Syst Res 77(3–4):315–327
15. Liao C-C (2010) Genetic k-means algorithm based RBF network for photovoltaic MPP prediction. Energy 35(2):529–536
16. Chen LR, Tsai CH, Lin YL, Lai YS (2010) A biological swarm chasing algorithm for tracking the PV maximum power point. IEEE Trans Energy Convers 25(2):484–493
17. Kadri R, Andrei H, Gaubert J-P, Ivanovici T, Champenois G, Andrei P (2012) Modeling of the photovoltaic cell circuit parameters for optimum connection model and real-time emulator with partial shadow conditions. Energy 42(1):57–67
18. Becherif M, Hissel D (2010) MPPT of a PEMFC based on air supply control of the motocompressor group. Int J Hydrogen Energy 35(22):12521–12530
19. Esram T, Kimball JW, Krein PT, Chapman PL, Midya P (2006) Dynamic maximum power point tracking of photovoltaic arrays using ripple correlation control. IEEE Trans Power Electron 21(5):1282–1291
20. Ariyur KB, Krstić M (2003) Real-time optimization by extremum-seeking control. Wiley, New York
21. Gelbert G, Moeck JP, Paschereit CO, King R (2012) Advanced algorithms for gradient estimation in one- and two-parameter extremum seeking controllers. J Process Control 22:700–709
22. Azar FE, Perrier M, Srinivasan B (2011) A global optimization method based on multi-unit extremum-seeking for scalar nonlinear systems. Comput Chem Eng 35:456–463
23. Manzie C, Krstić M (2009) Extremum seeking with stochastic perturbations. IEEE Trans Autom Control 54:580–585
24. Guay M, Dochain D, Perrier M (2004) Adaptive extremum seeking control of continuous stirred tank bioreactors with unknown growth kinetics. Automatica 40:881–888
25. Bizon N, Oproescu M, Raducu M, Constantinescu LM (2013) The extremum seeking control based on band pass filter for the dither signal processed in the control loop. Int J Tech Phys Probl Eng (IJTPE) 16(5/3):133–143

26. Bizon N (2013) Energy harvesting from the FC stack that operates using the MPP tracking based on modified extremum seeking control. Appl Energy 104:326–336
27. Bizon N (2013) FC energy harvesting using the MPP tracking based on advanced extremum seeking control. Int J Hydrogen Energy 38(4):1952–1966
28. Bizon N (2012) Distributed generation systems integrating renewable energy resources. Nova Science Publishers Inc., New York
29. Musio F et al (2011) PEMFC system simulation in MATLAB–Simulink® environment. Int J Hydrogen Energy 36(13):8045–8052
30. Linares JI, Herranz LE, Moratilla BY (2011) Maximum efficiency of direct energy conversion systems. Application to fuel cells. Int J Hydrogen Energy 36(18):11871–11885
31. Ahluwalia RK, Wang X (2005) Direct hydrogen fuel cell systems for hybrid vehicles. J Power Sources 139:152–164
32. Ahmed NA, Al-Othman AK, Al-Rashidi MR (2011) Development of an efficient utility interactive combined wind/photovoltaic/fuel cell power system with MPPT and DC bus voltage regulation. Electr Power Syst Res 81(5):1096–1106
33. Mehrdad E, Yimin G, Ali E (2010) Modern electric, hybrid electric, and fuel cell vehicles, vol 15. CRC Press, Boca Raton
34. Degrenne N, Buret F, Allard B, Bevilacqua P (2012) Electrical energy generation from a large number of microbial fuel cells operating at maximum power point electrical load. J Power Sources 205:188–193
35. Soltani M, Bathaee SMT (2010) Development of an empirical dynamic model for a Nexa PEM fuel cell power module. Energy Convers Manag 51(12):2492–2500
36. Ramos-Paja CA, Spagnuolo G, Petrone G, Giral R, Romero A (2010) Fuel cell MPPT for fuel consumption optimization. In: IEEE international symposium on circuits and systems, pp 2199–202
37. Giustiniani A, Petrone G, Spagnuolo G, Vitelli M (2010) Low-frequency current oscillations and maximum power point tracking in grid-connected fuel-cell-based systems. IEEE Trans Ind Electron 57(6):2042–2053
38. Bizon N, Radut M, Oproescu M (2015) Energy control strategies for the fuel cell hybrid power source under unknown load profile. Energy 86:31–41
39. Bizon N (2014) Load-following mode control of a standalone renewable/fuel cell hybrid power source. Energy Convers Manag 77:763–772
40. Krstić M (2000) Performance improvement and limitations in extremum seeking. Syst Control Lett 39(5):313–326
41. Krstić M, Wang H-H (2000) Design and stability analysis of extremum seeking feedback for general nonlinear systems. Automatica 36(2):595–601
42. Bizon N (2014) Tracking the maximum efficiency point for the FC system based on extremum seeking scheme to control the air flow. Appl Energy 129:147–157
43. Tirnovan R, Giurgea S (2012) Efficiency improvement of a PEMFC power source by optimization of the air management. Int J Hydrogen Energy 37(9):7745–7756
44. Segura F, Andújar JM (2012) Power management based on sliding control applied to fuel cell systems: a further step towards the hybrid control concept. Appl Energy 99:213–225
45. Wong KH et al (2011) A theoretical study of inlet relative humidity control in PEM fuel cell. Int J Hydrogen Energy 36(18):11871–11885
46. Bizon N, Oproescu M, Raceanu M (2015) Efficient energy control strategies for a standalone renewable/fuel cell hybrid power source. Energy Convers Manag 77:768–772
47. Bizon N (2014) Improving the PEMFC energy efficiency by optimizing the fuelling rates based on extremum seeking algorithm. Int J Hydrogen Energy 39(20):10641–10654
48. Loo KH, Zhu GR, Lai YM, Tse CK (2011) Development of a maximum-power-point tracking algorithm for direct methanol fuel cell and its realization in a fuel cell/supercapacitor hybrid energy system. In: 8th international conference on power electronics and ECCE Asia, pp 1753–1760

49. Woodward L, Perrier M, Srinivasan B, Pinto RP, Tartakovsky B (2010) Comparison of real-time methods for maximizing power output in microbial fuel cells. AIChE J 56(10):2742–2750
50. Woo CH, Benziger JB (2007) PEM fuel cell current regulation by fuel feed control. Chem Eng Sci 62:957–968
51. Zhang C, Ordóñez R (2012) Extremum-seeking control and applications: a numerical optimization-based approach. Springer, London
52. Bizon N (2010) On tracking robustness in adaptive extremum seeking control of the fuel cell power plants. Appl Energy 87(10):3115–3130
53. Chang YA, Moura SJ (2009) Air flow control in fuel cell systems: an extremum seeking approach. In: American Control Conference, pp 1052–1059
54. Bower W, Whitaker C (2002) Certification of photovoltaic inverters: the initial step toward PV system certification. In: IEEE conference photovoltaic specialists, pp 1406–1409
55. Zhong Z-D, Huo H-B, Zhu X-J, Cao G-Y, Ren Y (2008) Adaptive maximum power point tracking control of fuel cell power plants. J Power Sources 176:259–269
56. Tang Y, Yuan W, Pan M, Li Z, Chen G, Li Y (2010) Experimental investigation of dynamic performance and transient responses of a kW-class PEM fuel cell stack under various load changes. Appl Energy 87:1410–1417
57. Ramos-Paja CA, Giral R, Martinez-Salamero L, Romano J, Romero A, Spagnuolo G (2010) A PEM fuel-cell model featuring oxygen-excess-ratio estimation and power-electronics interaction. IEEE Trans Ind Electron 57(6):1914–1924
58. Springer TE, Zawodzinski TA, Gottesfeld S (1991) Polymer electrolyte fuel cell model. J Electrochem Soc 138(8):2334–2342
59. Wang Y, Chen KS, Mishler J, Cho SC, Adroher XC (2011) A review of polymer electrolyte membrane fuel cells: technology, applications, and needs on fundamental research. Appl Energy 88(4):981–1007
60. Gou B, Na WK, Diong B (2010) Fuel cells: modeling, control, and applications, vol 6. CRC Press, New York
61. Larminie J, Dicks A (2000) Fuel cell systems explained, 1st edn. Wiley, Chichester
62. Zenith F, Skogestad S (2007) Control of fuel cell power output. J Process Control 17:333–347
63. Pukrushpan JT, Stefanopoulou AG, Peng H (2004) Control of fuel cell power systems: principles, modeling and analysis and feedback design. Springer, London
64. Wahdame B, Candusso D, Kauffmann J-M (2006) Study of gas pressure and flow rate influences on a 500 W PEM fuel cell, thanks to the experimental design methodology. J Power Sources 156:92–99
65. Kolavennu PK, Palanki S, Cartes DA, Telotte JC (2008) Adaptive controller for tracking power profile in a fuel cell powered automobile. J Process Control 18:558–567
66. Bao C, Ouyang M, Yi B (2006) Modeling and control of air stream and hydrogen flow with recirculation in a PEM fuel cell system—II. Linear and adaptive nonlinear control. Int J Hydrogen Energy 31:1897–1913
67. Choe S-Y (2008) Dynamic simulator and controls for a PEM fuel cell power system. World Electr Veh J 2(3):46–62
68. Kunusch C, Puleston PF, Mayosky MA, Riera J (2009) Sliding mode strategy for PEM fuel cells stacks breathing control using a super-twisting algorithm. IEEE Trans Control Syst Technol 17(1):167–173
69. Feroldi D, Serra M, Riera J (2009) Energy management strategies based on efficiency map for fuel cell hybrid vehicles. J Power Sources 190:387–401
70. Dochain D, Perrier M, Guay M (2011) Extremum seeking control and its application to process and reaction systems: a survey. Math Comput Simul 82:369–380
71. Chen P-C (2011) The dynamics analysis and controller design for the PEM fuel cell under gas flow rate constraints. Int J Hydrogen Energy 36(4):3110–3122

72. Chen P-C (2011) Output-feedback voltage tracking control for input-constrained PEM fuel cell systems. Int J Hydrogen Energy 36(22):14608–14621
73. Tan Y, Nesic D, Mareels I (2006) On non-local stability properties of extremum seeking control. Automatica 42(6):889–903
74. Tan Y, Nesic D, Mareels I (2008) On the choice of dither in extremum seeking systems: a case study. Automatica 44:1446–1450